SIMULATION OF SUSPENDED SEDIMENT AND CONTAMINANT
TRANSPORT IN SHALLOW WATER USING TWO-DIMENSIONAL
DEPTH-AVERAGED MODEL WITH UNSTRUCTURED MESHES

BY

ZHENDUO ZHU

THESIS

Submitted in partial fulfillment of the requirements
for the degree of Master of Science in Civil Engineering
in the Graduate College of the
University of Illinois at Urbana-Champaign, 2011

Urbana, Illinois

Adviser:

Professor Marcelo H. García

ABSTRACT

With growing global populations and human activities, the problems of sediment transport and environmental hydraulics have been becoming more and more important and valued. Computational fluid dynamics is a very useful and powerful tool in those studies. In 2008, Dr. Liu developed a two-dimensional model HydroSed which solves for 2D shallow water equations and sediment bedload transport equation at Hydrosystems Laboratory, UIUC. In this thesis, the author further modifies and improves the HydroSedv1.0 model so that the model is able to deal with the transport of contaminant. In addition, the transport of suspended sediment is added and it is coupled with bed evolution.

The 2D advection-diffusion equation with source/sink terms is solved by finite volume method using Godunov scheme explicitly on unstructured meshes. Roe's approach is used to solve Riemann problem because the analytical solver is much computationally slower. Slope-limiter approaches are applied in order to get higher accuracy. Several pure advection tests are simulated to evaluate the performance of the model and the effect of different slope-limiter approaches. Furthermore, a dye-tracer study in the Chicago River is simulated for verifying the model in a real-world project. The numerical results show satisfactory matches with the field measurement data. A widely used three-dimensional model EFDC is also used for comparison. Both pure advection tests and dye-tracer study demonstrate that the performance of the model is satisfactory.

The model is applied to study the potential impacts of planned hydraulic structures in the Cañar River, Ecuador. The effects to both water flow during flood and sediment transport are studied. Due to the lack of field data in terms of water surface elevation, flow discharges and velocities in this river, the HydroSed model can help to a large extent to understand the problem and work together with a 1D model and other techniques for optimized designs.

To my family, for their consistent understanding and support.

ACKNOWLEDGMENTS

TABLE OF CONTENTS

CHAPTER 1

INTRODUCTION

Numerical modelling is a very important and useful approach in the study of environmental hydraulics and sediment transport which have been becoming more and more valued in the context of civil and hydraulic engineering practice (MacArthur et al. [1]). Researchers have put a lot of efforts and many 1D, 2D or 3D numerical models have been developed in those study areas. Although three-dimensional models are able to give more information about the turbulent flows and the vertical variety, they may need huge computational efforts (Liu and Garcia [2]). However, two-dimensional models are relatively computational faster and also are able to deal with more complicated problems and provide more details than one-dimensional models.

1.1   A Review of Existing 2D Models

Many 2D flow models with contaminant transport or sediment transport have been done. The review and comments of recent models are as follow. Sladkevich et al. ([3]) developed 2D and 3D models to simulate the contaminant transport phenomena in shallow aquatic environment. In the 2D model, shallow water equations were solved without considering turbulence model. Wu ([4]) solved flow equations, bedload and suspended load transport by using finite volume method on a curvilinear non-orthogonal grid. The depth-averaged parabolic model and the standard $k - \epsilon$ turbulence model were applied. Hudson and Sweby built a model to simulate bed load transport ([5]). A high-resolution scheme based on Roe's scheme is used. Murillo et al. ([6], [7]) solved coupled shallow water and solute flow equations by using upwind scheme based on finite volume method. Castro-Díaz et al. ([8]) developed a 2D model solving for coupled flow equations and sediment bedload transport equations based on a second order finite volume approach

on unstructured meshes. Kimura et al. ([9]) modelled suspended sediment transport in a shallow side-cavity. The depth-averaged parabolic turbulence model was employed and the effects of secondary currents were considered. As far as turbulence model is concerned, Nadaoka and Yagi ([10]) developed a SDS (sub-depth scale) turbulence model to simulate the evolution of horizontal large-scale eddies in shallow water and showed that the SDS model can predict turbulence-mixing better than the $k - \epsilon$ model.

In 2008, Liu et al. ([11]) developed a two-dimensional depth-averaged model, HydroSed, which solved shallow water equations and sediment bed-load transport equation. The equations were solved by finite volume method on unstructured meshes. This thesis improves the HydroSed model in order to simulate the transport of contaminant and suspended sediment. The 2D advection-diffusion equation with source/sink terms is solved by finite volume method using Godunov scheme explicitly on unstructured meshes. Roe's approach is used to solve Riemann problem. Slope-limiter approaches are applied in order to get higher accuracy. The modified model is well tested and applied to study the sediment transport problem in the Cañar River in Ecuador.

1.2 Thesis Outline

The thesis is organized as follow:

Chapter 2 presents the derivation of governing equations used in the model.

Chapter 3 explains the numerical schemes based on finite volume method.

Chapter 4 verifies the modified HydroSed model by using several pure advection tests and a dye-tracer study in the Chicago River.

Chapter 5 presents the application of the model in the Cañar River in Ecuador.

Chapter 6 proposes possible future work after summarizing conclusions from this study.

CHAPTER 2

GOVERNING EQUATIONS

2.1   2D Shallow Water Flow Model

The governing equations for water flow in a 2D depth-averaged model are derived from the 3D governing equations.

2.1.1   3D Flow Equations

The mass conservation equation is derived according to the relation that in a control volume the change of fluid mass is equal to the net inflow rate of mass.

$$\frac{d}{dt} \int_{\Omega} \rho dV = - \int_{S} \rho \mathbf{u} \cdot \mathbf{n} dA \tag{2.1}$$

The control volume is fixed in space, so the equation can be rewritten as:

$$\int_{\Omega} \frac{\partial \rho}{\partial t} dV + \int_{S} \rho \mathbf{u} \cdot \mathbf{n} dA = 0 \tag{2.2}$$

Note that according to Gauss's theorem,

$$\int_{S} \rho \mathbf{u} \cdot \mathbf{n} dA = \int_{\Omega} \nabla \cdot (\rho \mathbf{u}) \, dV \tag{2.3}$$

So,

$$\int_{\Omega} \left(\frac{\partial \rho}{\partial t} + \nabla \cdot (\rho \mathbf{u}) \right) dV = 0 \tag{2.4}$$

The above expression should be true anywhere and for any volume. Therefore,

$$\frac{\partial \rho}{\partial t} + \nabla \cdot (\rho \mathbf{u}) = 0 \tag{2.5}$$

If density ρ can be taken as a constant, e.g. incompressible fluid, the continuity equation reduces to

$$\nabla \cdot \mathbf{u} = 0 \tag{2.6}$$

According to the momentum conservation, the time rate of change of total momentum in control volume is equal to the sum of the net momentum flux across boundary of the control volume, the body forces action and surface forces action.

$$\frac{d}{dt} \int_{\Omega} \rho \mathbf{u} dV = - \int_{\partial \Omega} (\rho \mathbf{u}) \mathbf{u} \cdot \mathbf{n} dA + \int_{\Omega} \rho \mathbf{f}_b dV + \int_{\partial \Omega} \tau \cdot \mathbf{n} dA \tag{2.7}$$

Applying Gauss's theorem gives

$$\frac{d}{dt} \int_{\Omega} \rho \mathbf{u} dV + \int_{\Omega} \nabla \cdot (\rho \mathbf{u} \mathbf{u}) dV - \int_{\Omega} \rho \mathbf{f}_b dV - \int_{\Omega} \nabla \cdot \tau dV = 0 \tag{2.8}$$

Assuming that $\rho \mathbf{u}$ is smooth, the Leibniz integral can be used herein.

$$\int_{\Omega} \left(\frac{\partial (\rho \mathbf{u})}{\partial t} + \nabla \cdot (\rho \mathbf{u} \mathbf{u}) - \rho \mathbf{f}_b - \nabla \cdot \tau \right) dV = 0 \tag{2.9}$$

The formula should satisfy for arbitrary control volume, so

$$\frac{\partial (\rho \mathbf{u})}{\partial t} + \nabla \cdot (\rho \mathbf{u} \mathbf{u}) - \rho \mathbf{f}_b - \nabla \cdot \tau = 0 \tag{2.10}$$

That is,

$$\frac{\partial (\rho u_i)}{\partial t} + \frac{\partial}{\partial x_j} (\rho u_i u_j) = \rho f_{b_i} + \frac{\partial \tau_{ji}}{\partial x_j} \tag{2.11}$$

Similarly, if ρ is constant,

$$\frac{\partial \mathbf{u}}{\partial t} + \nabla \cdot (\mathbf{u} \mathbf{u}) - \mathbf{f}_b - \frac{1}{\rho} \nabla \cdot \tau = 0 \tag{2.12}$$

Or,

$$\frac{\partial u_i}{\partial t} + \frac{\partial}{\partial x_j} (u_i u_j) = f_{b_i} + \frac{1}{\rho} \frac{\partial \tau_{ji}}{\partial x_j} \tag{2.13}$$

Gravity is one kind of body forces. Other body forces may include Coriolis

force, et al. In surface forces term, for a Newtonian fluid, we know that

$$\tau_{ij} = -p\delta_{ij} + \mu \left(\frac{\partial u_i}{\partial x_j} + \frac{\partial u_j}{\partial x_i} \right) \tag{2.14}$$

Substituting it into the momentum equation for constant ρ gives:

$$\frac{\partial u_i}{\partial t} + \frac{\partial}{\partial x_j} (u_i u_j) = -\frac{1}{\rho} \frac{\partial p}{\partial x_i} + f_{b_i} + \nu \frac{\partial^2 u_i}{\partial x_j \partial x_j} \tag{2.15}$$

2.1.2   3D Reynolds-averaged Flow Equations

Considering the turbulence phenomenon, Reynolds decomposition is expressed as

$$u_i = \overline{u}_i + u_i{}' \tag{2.16}$$

where $u_i{}'$ represent fluctuation velocities and $\overline{u}_i$ represent Reynolds-averaged velocities. Applying Reynolds averaging to continuity equation for incompressible Newtonian flow gives:

$$\nabla \cdot \overline{\mathbf{u}} = 0 \tag{2.17}$$

$$\nabla \cdot \mathbf{u}' = 0 \tag{2.18}$$

Similarly, the momentum equations for incompressible Newtonian flow can be reduced to

$$\frac{\partial \overline{u}_i}{\partial t} + \frac{\partial}{\partial x_j} (\overline{u_i u_j}) = -\frac{1}{\rho} \frac{\partial p}{\partial x_i} + f_{b_i} + \nu \frac{\partial^2 \overline{u}_i}{\partial x_j \partial x_j} \tag{2.19}$$

That is,

$$\frac{\partial \overline{u}_i}{\partial t} + \frac{\partial}{\partial x_j} (\overline{u}_i \overline{u}_j) = -\frac{1}{\rho} \frac{\partial p}{\partial x_i} + f_{b_i} + \nu \frac{\partial^2 \overline{u}_i}{\partial x_j \partial x_j} - \frac{\partial}{\partial x_j} \left(\overline{u_i{}' u_j{}'} \right) \tag{2.20}$$

$$\frac{\partial \overline{u}_i}{\partial t} + \overline{u}_j \frac{\partial \overline{u}_i}{\partial x_j} = -\frac{1}{\rho} \frac{\partial}{\partial x_j} \left(p\delta_{ij} + \rho \overline{u_i{}' u_j{}'} - \mu \frac{\partial \overline{u}_i}{\partial x_j} \right) + f_{b_i} \tag{2.21}$$

Usually for simplicity, the "bar" is omitted and the term of Reynolds

stresses $-\rho\overline{u_i'u_j'}$ is expressed as τ_{ij}.

To sum up, the Reynolds-Averaged continuity equation is expressed as

$$\frac{\partial u_i}{\partial x_i} = 0 \tag{2.22}$$

The Reynolds-Averaged momentum equations are

$$\frac{\partial u_i}{\partial t} + u_j \frac{\partial u_i}{\partial x_j} = -\frac{1}{\rho}\frac{\partial p}{\partial x_i} + \frac{\partial}{\partial x_j}\left(\tau_{ij} + \nu\frac{\partial u_i}{\partial x_j}\right) + f_{b_i} \tag{2.23}$$

Considering that

$$\tau_{ij} = \nu_T \frac{\partial u_i}{\partial x_j}$$

We can get

$$\frac{\partial u_i}{\partial t} + u_j \frac{\partial u_i}{\partial x_j} = -\frac{1}{\rho}\frac{\partial p}{\partial x_i} + (\nu_T + \nu)\frac{\partial^2 u_i}{\partial x_j \partial x_j} + f_{b_i} \tag{2.24}$$

2.1.3 2D Depth-averaged Flow Equations

When vertical characteristics are relatively not important in evaluating the behavior of water flows, the depth averaged 2D model can be used to simplify the problem. In Cartesian coordinate system,

$$\overline{u}_i = \frac{1}{h}\int_0^h u_i dz \tag{2.25}$$

where $i = 1$, 2 which correspond to the two components in horizontal direction.

The integral of continuity equation gives:

$$\int_0^h \left(\frac{\partial u_1}{\partial x_1} + \frac{\partial u_2}{\partial x_2} + \frac{\partial u_3}{\partial x_3}\right) dx_3 = 0 \tag{2.26}$$

$$\frac{\partial}{\partial x_1}\int_0^h u_1 dx_3 + \frac{\partial}{\partial x_2}\int_0^h u_2 dx_3 + u_3|_0^h = 0 \tag{2.27}$$

$$\frac{\partial(h\overline{u}_i)}{\partial x_i} + \frac{\partial h}{\partial t} = 0 \tag{2.28}$$

6

The integrals of momentum equations show:

$$\int_0^h \frac{\partial u_i}{\partial t} dx_3 + \int_0^h \frac{\partial u_i u_j}{\partial x_j} dx_3 = -\frac{1}{\rho} \int_0^h \frac{\partial}{\partial x_j} \left(p\delta_{ij} - \tau_{ij} - \mu \frac{\partial u_i}{\partial x_j} \right) dx_3 +$$
$$\int_0^h f_{b_i} dx_3 \quad (2.29)$$

Note that

$$p = p(z) = \rho g h$$

One can get

$$\frac{\partial (h\overline{u}_i)}{\partial t} + \frac{\partial}{\partial x_j} \int_0^h u_i u_j dx_3 = -gh\frac{\partial h}{\partial x_i} + \nu\frac{\partial (h\overline{u}_i)}{\partial x_j \partial x_j} + \frac{1}{\rho}\frac{\partial}{\partial x_j} \int_0^h \tau_{ij} dx_3 +$$
$$\frac{\tau_s^i - \tau_b^i}{\rho} + h f_i \quad (2.30)$$

$$\frac{\partial (h\overline{u}_i)}{\partial t} + \frac{\partial (h\overline{u}_i\overline{u}_j)}{\partial x_j} = \frac{\partial (h\overline{u}_i\overline{u}_j)}{\partial x_j} - \frac{\partial}{\partial x_j} \int_0^h u_i u_j dx_3 - gh\frac{\partial h}{\partial x_i} +$$
$$\nu\frac{\partial (h\overline{u}_i)}{\partial x_j \partial x_j} + \frac{1}{\rho}\frac{\partial}{\partial x_j} \int_0^h \tau_{ij} dx_3 + \frac{\tau_s^i - \tau_b^i}{\rho} + h f_i \quad (2.31)$$

$$\frac{\partial (h\overline{u}_i)}{\partial t} + \frac{\partial (h\overline{u}_i\overline{u}_j)}{\partial x_j} = -\frac{\partial}{\rho\partial x_j} \int_0^h \rho (u_i - \overline{u}_i)(u_j - \overline{u}_j) dx_3 - gh\frac{\partial h}{\partial x_i} +$$
$$\nu\frac{\partial (h\overline{u}_i)}{\partial x_j \partial x_j} + \frac{1}{\rho}\frac{\partial}{\partial x_j} \int_0^h \tau_{ij} dx_3 + \frac{\tau_s^i - \tau_b^i}{\rho} + h f_i \quad (2.32)$$

Using U, V as the notation of depth-averaged velocity at x, y direction respectively, the continuity and momentum equations are

$$\frac{\partial h}{\partial t} + \frac{\partial (hU)}{\partial x} + \frac{\partial (hV)}{\partial y} = 0 \tag{2.33}$$

$$\frac{\partial (hU)}{\partial t} + \frac{\partial (hUU)}{\partial x} + \frac{\partial (hUV)}{\partial y} = -\frac{\partial}{\rho \partial x_j} \int_0^h \rho (u_i - \overline{u}_i)(u_j - \overline{u}_j) \, dx_3$$
$$-gh\frac{\partial h}{\partial x} + \nu \frac{\partial (hU)}{\partial x_j \partial x_j} + \frac{1}{\rho}\frac{\partial}{\partial x_j}\int_0^h \tau_{ij} dx_3 + \frac{\tau_s^1 - \tau_b^1}{\rho} + hf_1 \tag{2.34}$$

$$\frac{\partial (hV)}{\partial t} + \frac{\partial (hVU)}{\partial x} + \frac{\partial (hVV)}{\partial y} = -\frac{\partial}{\rho \partial x_j} \int_0^h \rho (u_i - \overline{u}_i)(u_j - \overline{u}_j) \, dx_3$$
$$-gh\frac{\partial h}{\partial y} + \nu \frac{\partial (hV)}{\partial x_j \partial x_j} + \frac{1}{\rho}\frac{\partial}{\partial x_j}\int_0^h \tau_{ij} dx_3 + \frac{\tau_s^2 - \tau_b^2}{\rho} + hf_2 \tag{2.35}$$

Neglecting the turbulence term, dispersion term and viscous tem, the normal 2D shallow water equations can be got as:

$$\frac{\partial h}{\partial t} + \frac{\partial (hU)}{\partial x} + \frac{\partial (hV)}{\partial y} = 0 \tag{2.36}$$

$$\frac{\partial (hU)}{\partial t} + \frac{\partial (hUU)}{\partial x} + \frac{\partial (hUV)}{\partial y} = -gh\frac{\partial h}{\partial x} + \frac{\tau_s^1 - \tau_b^1}{\rho} + hf_1 \tag{2.37}$$

$$\frac{\partial (hV)}{\partial t} + \frac{\partial (hVU)}{\partial x} + \frac{\partial (hVV)}{\partial y} = -gh\frac{\partial h}{\partial y} + \frac{\tau_s^2 - \tau_b^2}{\rho} + hf_2 \tag{2.38}$$

Considering the viscous term and the Coriolis force, the original HydroSed2D model gives:

$$\frac{\partial h}{\partial t} + \frac{\partial (hU)}{\partial x} + \frac{\partial (hV)}{\partial y} = 0 \tag{2.39}$$

$$\frac{\partial\left(hU\right)}{\partial t} + \frac{\partial\left(hUU\right)}{\partial x} + \frac{\partial\left(hUV\right)}{\partial y} - \nu\left(\frac{\partial^2\left(hU\right)}{\partial x^2} + \frac{\partial^2\left(hU\right)}{\partial y^2}\right) =$$
$$-gh\frac{\partial h}{\partial x} + \frac{\tau_s^1 - \tau_b^1}{\rho} + hfV \tag{2.40}$$

$$\frac{\partial\left(hV\right)}{\partial t} + \frac{\partial\left(hVU\right)}{\partial x} + \frac{\partial\left(hVV\right)}{\partial y} - \nu\left(\frac{\partial^2\left(hV\right)}{\partial x^2} + \frac{\partial^2\left(hV\right)}{\partial y^2}\right) =$$
$$-gh\frac{\partial h}{\partial y} + \frac{\tau_s^2 - \tau_b^2}{\rho} - hfU \tag{2.41}$$

where f is the Coriolis parameter.

The author modified the original model to consider the turbulent term by applying the depth-averaged parabolic model.

$$\frac{\partial\left(hU\right)}{\partial t} + \frac{\partial\left(hUU\right)}{\partial x} + \frac{\partial\left(hUV\right)}{\partial y} - (\nu + \nu_T)\left(\frac{\partial^2\left(hU\right)}{\partial x^2} + \frac{\partial^2\left(hU\right)}{\partial y^2}\right) =$$
$$-gh\frac{\partial h}{\partial x} + \frac{\tau_s^1 - \tau_b^1}{\rho} + hfV \tag{2.42}$$

$$\frac{\partial\left(hV\right)}{\partial t} + \frac{\partial\left(hVU\right)}{\partial x} + \frac{\partial\left(hVV\right)}{\partial y} - (\nu + \nu_T)\left(\frac{\partial^2\left(hV\right)}{\partial x^2} + \frac{\partial^2\left(hV\right)}{\partial y^2}\right) =$$
$$-gh\frac{\partial h}{\partial y} + \frac{\tau_s^2 - \tau_b^2}{\rho} - hfU \tag{2.43}$$

where

$$\nu_T = \alpha_T h u_*$$

u_* is the bed shear velocity; h is water depth; U and V are depth-averaged velocities in the x and y directions; ν is water viscosity; ν_T is turbulent viscosity; g is gravity; τ_s^1 and τ_s^2 are surface shear stresses caused by wind in x and y directions; τ_b^1 and τ_b^2 are bed shear stresses in x and y directions.

2.2 Contaminant Transport Model

The equation to describe the transport phenomena in shallow water is the two-dimensional advection-diffusion equation with source/sink term which is shown below. The details of derivation can be found in Elder's book ([12]).

$$
\frac{\partial (hC)}{\partial t} + \frac{\partial (hUC)}{\partial x} + \frac{\partial (hVC)}{\partial y} = \frac{\partial}{\partial x} \left(hD_{xx} \frac{\partial C}{\partial x} \right) +
$$
$$
\frac{\partial}{\partial y} \left(hD_{yy} \frac{\partial C}{\partial y} \right) + \frac{\partial}{\partial x} \left(hD_{xy} \frac{\partial C}{\partial y} \right) + \frac{\partial}{\partial y} \left(hD_{yx} \frac{\partial C}{\partial x} \right) + Q_c
$$

(2.44)

where C is the depth-averaged concentration; D_{xx}, D_{yy}, D_{xy} and D_{yx} are the components of generalized effective diffusion tensor; Q_c is the source/sink term or some expression for the decay of contaminant.

There are two options available in the current model to deal with the dispersion coefficients. One way is to specify those coefficients artificially. In this way, those coefficients are taken actually like calibration parameters. The other way is to use the follow formulas [3].

$$
D_{ij} = \varepsilon_s \delta_{ij} + D_h \frac{q_i q_j}{q^2}
$$

(2.45)

where i, j correspond to x and y respectively; δ_{ij} is Kronecker's delta; and

$$
q_x = hU
$$

(2.46)

$$
q_y = hV
$$

(2.47)

$$
q = \sqrt{q_x^2 + q_y^2}
$$

(2.48)

$$
D_h = 5.86\sqrt{\lambda}q
$$

(2.49)

$$
\varepsilon_s = 0.22\sqrt{\lambda}q
$$

(2.50)

$$
\lambda = gn^2 h^{-1/3}
$$

(2.51)

where n is Manning's roughness coefficient.

2.3 Sediment Transport and River Morphodynamics Model

With growing global populations and human activities, the sediment transport problem has been becoming more and more important and valued, especially in the context of civil and hydraulic engineering practice ([13]). Based on the mechanism of transport, sediment transport load is divided into bed load and suspended load. The original HydroSed2D model only takes the bed load in consideration. Thus, besides the calculation of contaminant transport, another important goal of this study is to incorporate suspended load module into the original HydroSed2D model, which is also coupled with morphodynamical equation.

There are two methods existing in the model to compute bedload transport: Grass formula ([14]) and Meyer-Peter and Muller formula ([15]).

2.3.1 Bedload Transport Equations

Grass Formula

$$q_{sx} = AU \left(U^2 + V^2 \right)^{\frac{m-1}{2}} \tag{2.52}$$

$$q_{sy} = AV \left(U^2 + V^2 \right)^{\frac{m-1}{2}} \tag{2.53}$$

where A and m are parameters. For fine sand, $A = 0.001$ and $m = 3$ are recommended.

Advantage of the Grass method is that this method can be easily used in numerical models, because it directly links the bed transport rates to velocities by applying the two parameters, A and m. Problems of this method may be the uncertainties and difficulties in the evaluation of the parameters A and m. Also, in this method, as long as the velocities are larger than zero, there will always be sediment bed load transport, thus, threshold condition for sediment movement is can not be considered using Grass method.

Meyer-Peter and Muller Formula

$$q^* = 8(\tau^* - \tau_c^*)^{3/2} \tag{2.54}$$

where

$$\tau_c^* = 0.047 \tag{2.55}$$

$$q^* = \frac{q_b}{D\sqrt{gRD}} \tag{2.56}$$

$$\tau^* = \frac{\tau_b}{\rho g R D} \tag{2.57}$$

$$q_{sx} = q_b \frac{\tau_x}{\tau_b} \tag{2.58}$$

$$q_{sy} = q_b \frac{\tau_y}{\tau_b} \tag{2.59}$$

2.3.2 Suspended Load Transport Equations

The 2D depth-averaged equation for suspended transport can be expressed as follow:

$$
\begin{aligned}
\frac{\partial (hC)}{\partial t} + \frac{\partial (hUC)}{\partial x} + \frac{\partial (hVC)}{\partial y} &= \frac{\partial}{\partial x}\left(hD_{xx}\frac{\partial C}{\partial x}\right) + \frac{\partial}{\partial y}\left(hD_{yy}\frac{\partial C}{\partial y}\right) \\
&+ \frac{\partial}{\partial x}\left(hD_{xy}\frac{\partial C}{\partial y}\right) + \frac{\partial}{\partial y}\left(hD_{yx}\frac{\partial C}{\partial x}\right) + v_s\left(E_s - c_b\right) + Q_c
\end{aligned}
\tag{2.60}
$$

It can be found that the governing equation for suspended load transport is similar to the one for contaminant transport. They share the same advection and diffusion terms. The only difference is that the suspended load transport equation has two terms corresponding to the interaction between the flow and the bed: sediment entrainment rate and deposition rate. The term Q_c is still in the equation in order to consider the boundary conditions or other source/sink terms. v_s is the sediment fall velocity which relates to the size of the sediment particles.

Deposition Rate

According to Parker et al. ([16]),

$$c_b = r_o C \tag{2.61}$$

$$r_o = 1 + 31.5 \left(\frac{u_*}{v_s} \right)^{-1.46} \tag{2.62}$$

where u_* is the shear velocity.

Entrainment Rate

The sediment entrainment rate is computed according to García and Parker ([17], [18]):

$$E_s = \frac{A Z_u^5}{1 + \frac{A}{0.3} Z_u^5} \tag{2.63}$$

where $A = 1.3\text{E-}7$

$$Z_u = \frac{u_{*s}}{v_s} R_{ep}^{0.6} \tag{2.64}$$

For fine-grained non-cohesive sediments and $R_{ep} < 3.5$,

$$Z_u = 0.708 \frac{u_*}{v_s} R_{ep}^{0.6} \tag{2.65}$$

$$R_{ep} = \frac{D\sqrt{gRD}}{\nu} \tag{2.66}$$

Note that u_{*s} is the shear velocity associated with skin friction.

$$u_{*s} = \sqrt{gH_s S} \tag{2.67}$$

where S is calculated according to Manning's formula:

$$S = n^2 \left(U^2 + V^2 \right) h^{-4/3} \tag{2.68}$$

$$H_s = \frac{h^{4/3}}{gn^2} \left(\frac{1}{\kappa} \ln \left(11 \frac{H_s}{k_s} \right) \right)^{-2} \tag{2.69}$$

13

where κ is the von Karman's constant, 0.4; $k_s = 2$D

2.3.3   River Morphological Equation

The 2D Exner's equation is used herein to calculate the river morphological changes due to the sediment transport.

$$(1 - \lambda_p) \frac{\partial z}{\partial t} + \left(\frac{\partial q_{sx}}{\partial x} + \frac{\partial q_{sy}}{\partial y} \right) = v_s \left(c_b - E_s \right) \tag{2.70}$$

where λ_p is the bed porosity.

CHAPTER 3

NUMERICAL METHODS

The governing equations are discretized using the finite volume method on unstructured meshes. The previous HydroSed2D model solved for shallow water equations, sediment bedload transport equations and the morphodynamical equation. The details of the numerical methods used in the previous model can be found in Liu et al. (2008) ([11]). The sediment bedload transport equation can be either coupled or decoupled with shallow water equations mainly depending on the speed of the scour process. Cao et al. (2002) ([19]) compared those two approaches and found that for slow scour process, both of them can give good evaluation while for fast scour coupled approach is needed. However, in natural rivers, mostly the scour is not so fast and the uncoupled approach allows use of different time scales for hydrodynamics and bed evolution which can make the simulation much faster. As shown in Chapter 2, the governing equations for contaminant transport and suspended load transport are both 2D advection-diffusion equations. The difference can be taken as only in the source/sink terms.

Since the change of density with the contaminant or suspended sediment concentration is not considered, the transport module can be physically decoupled with the shallow water equations. Therefore, the model will first solve the shallow water equations. After getting the velocities, i.e., the flow field, the transport module will be solved and the concentration at new time step will replace the one at old time step.

3.1   Finite Volume Method

The 2D advection-diffusion equation (2.44) can be reorganized as follow:

$$\frac{\partial (hC)}{\partial t} + \frac{\partial}{\partial x}\left(hUC - hD_{xx}\frac{\partial C}{\partial x} - hD_{xy}\frac{\partial C}{\partial y}\right) +$$
$$\frac{\partial}{\partial y}\left(hVC - hD_{yy}\frac{\partial C}{\partial y} - hD_{yx}\frac{\partial C}{\partial x}\right) = Q_c \tag{3.1}$$

Applying Gauss's theorem and integral through the mesh cell gives

$$\frac{\partial}{\partial t}\iint\limits_{\Omega} Q d\Omega + \oint\limits_{S} \mathbf{F}\cdot\mathbf{n}dS = \iint\limits_{\Omega} Q_c d\Omega \tag{3.2}$$

where

$$Q = hC\ ;\ \mathbf{F}\cdot\mathbf{n} = F^A - F^D = \left(f^A - f^D\right)n_x + \left(g^A - g^D\right)n_y;$$
$$f^A = hUC\ ;\ g^A = hVC\ ;\ f^D = hD_{xx}\frac{\partial C}{\partial x} + hD_{xy}\frac{\partial C}{\partial y}\ ;$$
$$g^D = hD_{yy}\frac{\partial C}{\partial y} + hD_{yx}\frac{\partial C}{\partial x}$$

where the superscript A represents advection terms and D represents diffusion terms. They are differentiated because they will be solved by different approaches.

In the first term on the left hand side and the term on the right hand side, Q and Q_c are taken as constant throughout one cell. Therefore,

$$\frac{\partial}{\partial t}\iint\limits_{\Omega} Q d\Omega = \frac{\partial (QA_\Omega)}{\partial t} \tag{3.3}$$

$$\iint\limits_{\Omega} Q_c d\Omega = Q_c A_\Omega \tag{3.4}$$

Explicit method is applied for temporal discretization.

$$\oint\limits_{S_i} \mathbf{F}\cdot\mathbf{n}dS = \sum_j \left(F_{i,j}{}^A - F_{i,j}{}^D\right)L_j \tag{3.5}$$

where L is the edge length in the computation cell.

For advection terms, Roe's approximate solver ([20], [21]) is used instead of the analytical solver of the Riemann problem. The Riemann problem comes out from the framework of Godunov ([22]). Godunov suggested using the explicit solution of the Riemann problems at cell interfaces to solve hyper-

bolic problems. The Riemann problem is related to a discontinuous initial distribution and theoretically is able to be solved analytically. However, the analytical solver is much slower. Thus, the model assumes a one dimensional Riemann problem in the direction normal to the cell interface edge, and solves it using Roe's flux function (as follows) instead:

$$F_{i,j}^A = \frac{1}{2} \left[F^A \left(Q_{i,j}{}^+ \right) + F^A \left(Q_{i,j}{}^- \right) - A \left(Q_{i,j}{}^+ - Q_{i,j}{}^- \right) \right] \qquad (3.6)$$

$$A = \frac{\partial \left(\mathbf{F} \cdot \mathbf{n} \right)}{\partial Q} = U n_x + V n_y \qquad (3.7)$$

where $Q_{i,j}^+$ and $Q_{i,j}^-$ are the values of Q on the downstream and upstream sides of the interface edge respectively. Note that the values of U and V are evaluated by Roe's average state shown below.

$$U = \frac{U^+ \sqrt{h^+} + U^- \sqrt{h^-}}{\sqrt{h^+} + \sqrt{h^-}} \qquad (3.8)$$

$$V = \frac{V^+ \sqrt{h^+} + V^- \sqrt{h^-}}{\sqrt{h^+} + \sqrt{h^-}} \qquad (3.9)$$

where the superscripts have the same meaning as the equation (3.6).

For the diffusion terms,

$\frac{\partial C}{\partial x}$ and $\frac{\partial C}{\partial y}$ on the cell-interface edge are evaluated by using the average value between two cells weighted by the area of each cell as follows.

$$\nabla C_{edge} = \frac{\nabla C^- A^+ + \nabla C^+ A^-}{A^+ + A^-} \qquad (3.10)$$

where the superscripts still have the same meaning as the equation (3.6).

3.2   Limiter for Higher Order Scheme

As mentioned above, the computation of advection terms need the values at the cell-interface edge. However, the variables are stored at the center of the cells and considered as constant throughout each cell in the simplest case. In order to get higher order accuracy, extrapolation is needed. One simple way is using piecewise linear assumption as follows.

$$Q(x, y) = Q_0 + \nabla Q_0 \cdot \mathbf{r} \tag{3.11}$$

where Q_0 is the cell center value; $\mathbf{r}$ is the vector from cell center to the any location we need.

However, in order to get second or higher order accuracy of data extrapolation, non-linear limiters are usually used. After applying non-linear limiters, the new extrapolation form is expressed as follows.

$$Q(x, y) = Q_0 + \Phi \nabla Q_0 \cdot \mathbf{r} \tag{3.12}$$

Compared with the equation (3.11), the new introduced parameter Φ is termed as "limiter". When it equals to 1, the form goes to the equation (3.11); when the limiter is set to 0, it goes to the piece-wise constant case.

There are many forms of limiters ([23]). The form applied in this model is the same as the one used by Anastasiou and Chan ([24]) which is defined as:

$$\Phi = \min (\Phi_j) \,; j = k(i) \tag{3.13}$$

$$\Phi_j (r_j) = \max \left[\min (\beta r_j, 1) , \min (r_j, \beta) \right] \tag{3.14}$$

$$r_j = \begin{cases} (Q_0^{\max} - Q_0) / (Q_j - Q_0) & \text{if } (Q_j - Q_0) > 0 \\ (Q_0^{\min} - Q_0) / (Q_j - Q_0) & \text{if } (Q_j - Q_0) < 0 \\ 1 & \text{if } (Q_j - Q_0) = 0 \end{cases} \tag{3.15}$$

$$Q_0^{\min} = \min (Q_0, Q_{neighbor}) \,; Q_0^{\max} = \max (Q_0, Q_{neighbor}) \tag{3.16}$$

$$Q_j = Q_0 + \nabla Q_0 \cdot \mathbf{r} \tag{3.17}$$

where β can be set as any values between 1 and 2. In particular, when β equals to 1, the form goes to minmod limiter and when β equals to 2, it goes to Superbee limiter. One important and interesting point of this method is that it allows trying something between by setting β to be something between 1 and 2, e.g. 1.5.

CHAPTER 4

MODEL VERIFICATION

4.1 Pure Advection Tests

Several pure advection tests are simulated in order to validate the model. The numerical results got by using different forms of limiters are shown and compared with the analytical solution and also with each other, to verify the effects of limiters on restricting numerical dispersion. The governing equation for pure advection test with initial concentration reduces to

$$\frac{\partial (hC)}{\partial t} + \frac{\partial}{\partial x} (hUC) + \frac{\partial}{\partial y} (hVC) = 0 \tag{4.1}$$

where h, U and V are all taken as constant.

4.1.1 Model Settings

The study domain is a 10 m by 10 m square. The regular triangular mesh is generated by using a commercial grid generation software GAMBIT (by ANSYS Inc.). The model so far can read the grid files generated by either GAMBIT or Gmsh (free to the public). The whole domain is firstly divided by 0.1 m by 0.1 m squares and then the squares are divided into triangular cell. Therefore, there are totally 20,000 cells and 10,201 nodes (see figure 4.1).

The initial concentration condition is set as

$$C = \begin{cases} 10 \ (1 < x < 3, \ 1 < y < 3) \\ \quad 0 \ \text{other places} \end{cases} \tag{4.2}$$

The water depth is taken as constant, h = 10m. Other important parameters are shown in table 4.1 below.
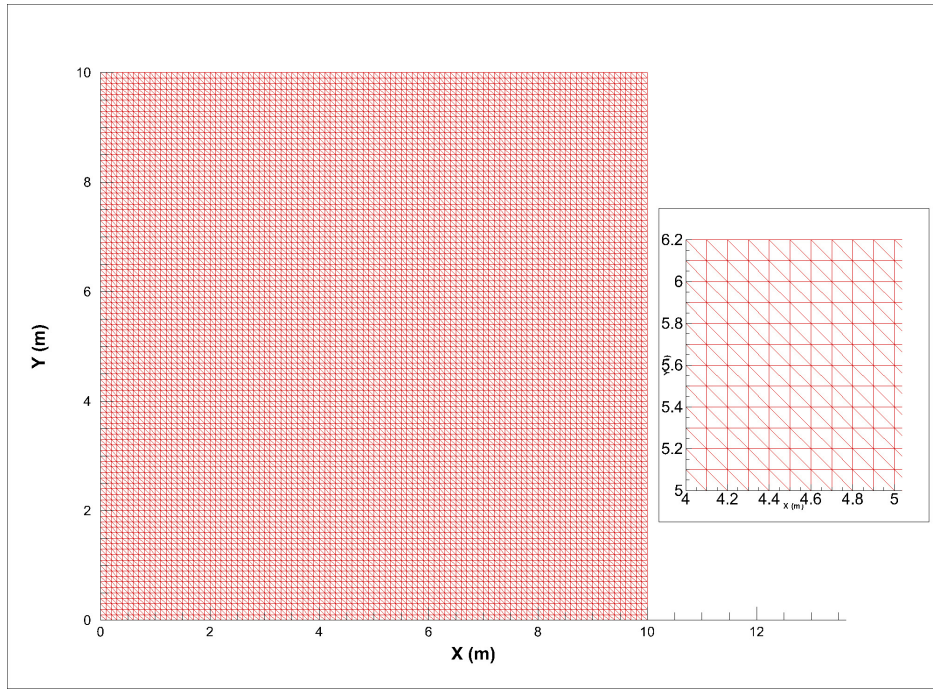
Figure 4.1: Unstructured meshes (20000 cells, 10201 nodes)
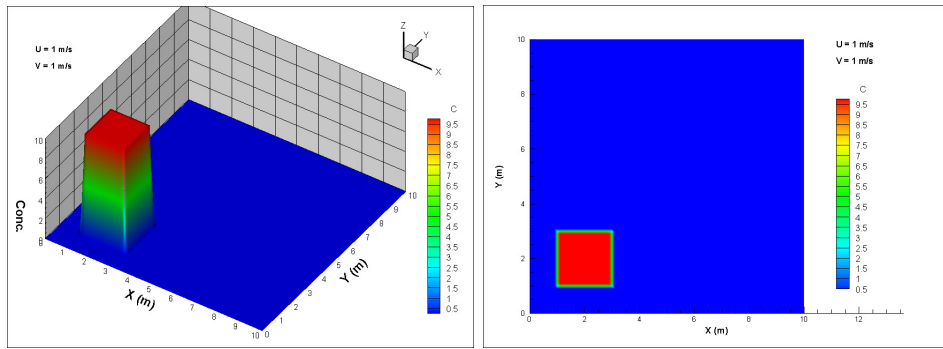
Figure 4.2: Initial concentration condition

Table 4.1: Time parameters in the numerical simulations

Time Step	0.0001 s
Starting Time	0 s
Ending Time	5 s
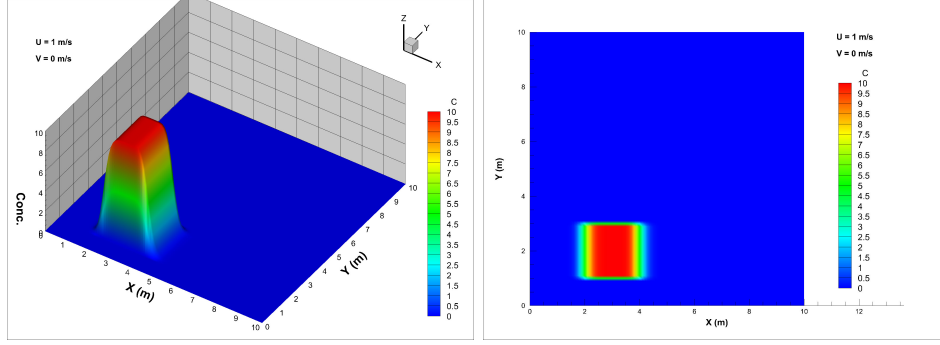
Figure 4.3: Numerical results of test 1 at t = 1s

Several different cases are simulated and the summary is shown in table 4.2 below.

Table 4.2: The summary of numerical tests

Test 1	U = 1.0; V = 0.0	$\Phi = 0$
Test 2	U = 1.0; V = 1.0	$\Phi = 0$
Test 3	U = 1.0; V = 1.0	minmod limiter ($\beta = 1$)
Test 4	U = 1.0; V = 1.0	Superbee limiter ($\beta = 2$)
Test 5	U = 1.0; V = 1.0	$\beta = 1.5$

4.1.2   Test 1

In test 1, the contaminant is supposed to move in only x direction with a constant speed 1.0 m/s. With $\Phi = 0$ which corresponds to upwind scheme, the numerical results are shown below in figures 4.3 to 4.7.

As expected, simulation results show that the transport rate in x direction is 1.0 m/s. However, there is obvious numerical dispersion. Instead of keeping the shape of square, the domain stretches in x-direction. The length of the domain in x direction is getting bigger and bigger and the peak is changing from platform to be sharper and lower. In the x-y plane, the domain shape changes from square shape to bell shape.

Several parameters are used to evaluate the performance of the numerical model. They are the maximum of concentration, minimum of concentration, mean absolute error, root mean square error and relative global mass error.

The mean absolute error (MAE), root mean square error (RMSE) and
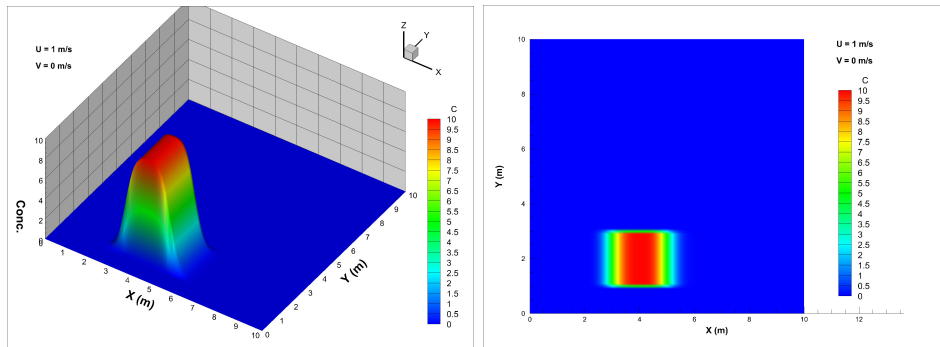
Figure 4.4: Numerical results of test 1 at t = 2s
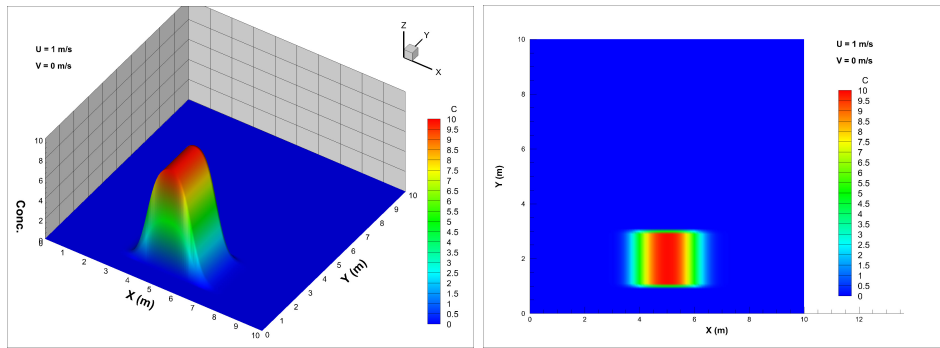
Figure 4.5: Numerical results of test 1 at t = 3s
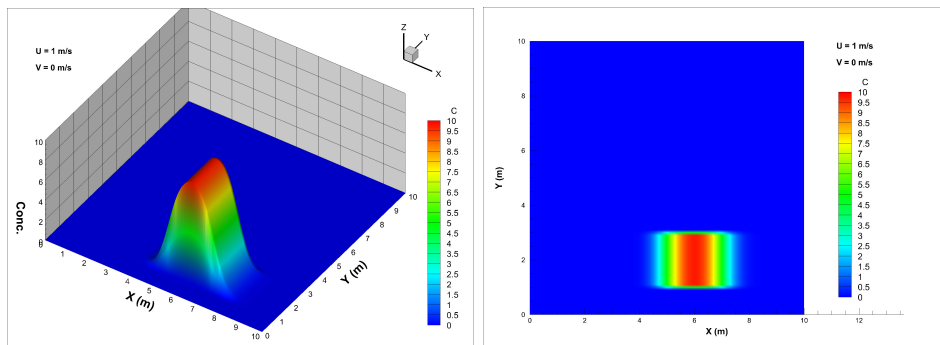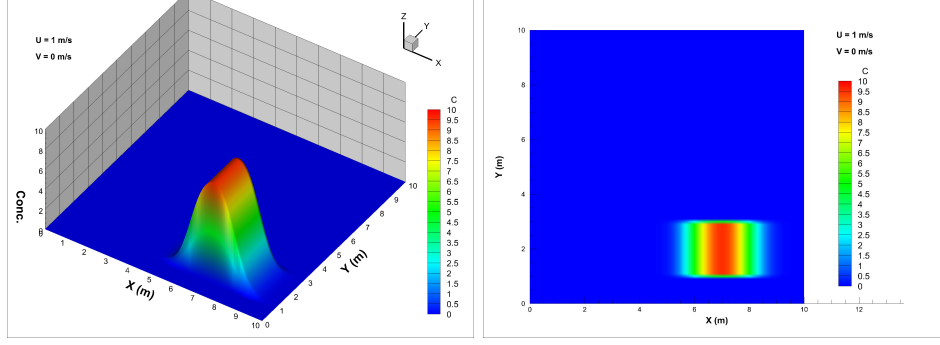

Figure 4.6: Numerical results of test 1 at t = 4s

Figure 4.7: Numerical results of test 1 at t = 5s

relative global mass error (RGME) are defined as

$$MAE = \frac{1}{n} \sum_{i=1}^{n} |f_i - y_i| \tag{4.3}$$

$$RMSE = \sqrt{\frac{1}{n} \sum_{i=1}^{n} (f_i - y_i)^2} \tag{4.4}$$

$$RGME = \frac{TotalMass_{numerical} - TotalMass_{analytical}}{TotalMass_{analytical}} \tag{4.5}$$

where n is the number of nodes (in order to see the results better in Tecplot software the concentration values are interpolated from cell centers to nodes); f_i is numerical results; y_i is analytical results. A test code is written using FORTRAN in order to calculate those parameters.

Table 4.3: The performance of numerical test 1

t(s)	C_{max}	C_{min}	Mean Absolute Error	Root Mean Square Error	Global Mass Relative Error
1	9.99989	-3.19E-25	0.05333	0.34560	-9.09E-16
2	9.98174	-6.60E-34	0.08149	0.44479	1.71E-15
3	9.89669	-1.28E-42	0.10336	0.50936	-3.52E-15
4	9.74089	-2.39E-51	0.12188	0.55882	-9.80E-13
5	9.53894	-5.17E-60	0.13824	0.60001	-2.51E-06

From the table 4.3 above we can see that the performance of global mass balance is very good which can also be seen in the later simulations. At t = 5s the global mass balance is relatively much bigger than the previous time steps because some mass is lost and out of the domain due to numerical dispersion. The maximum concentration is getting smaller and smaller. Even
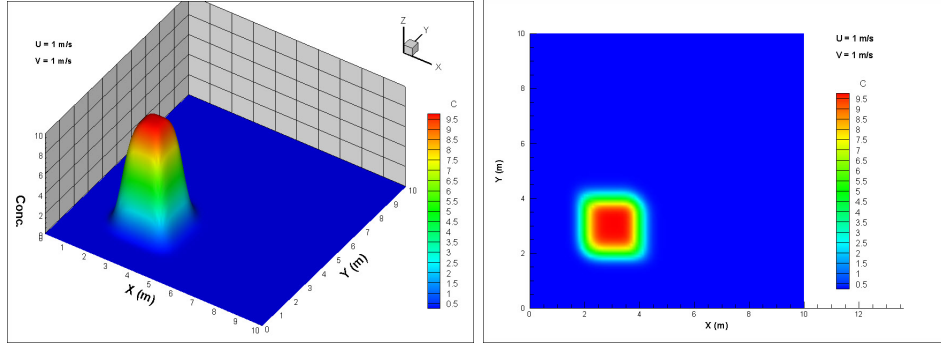
23

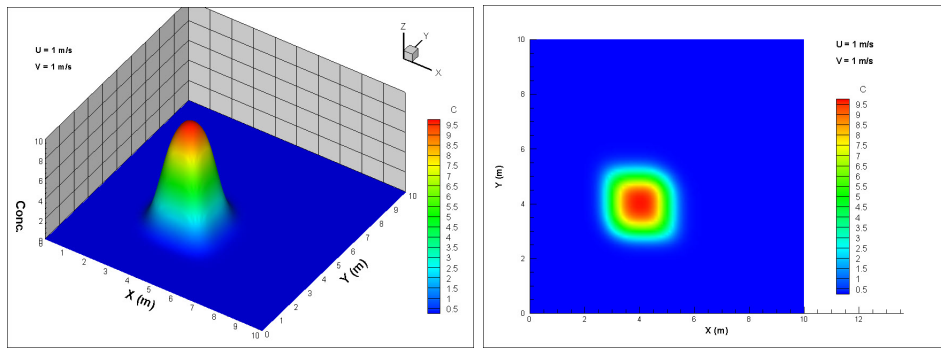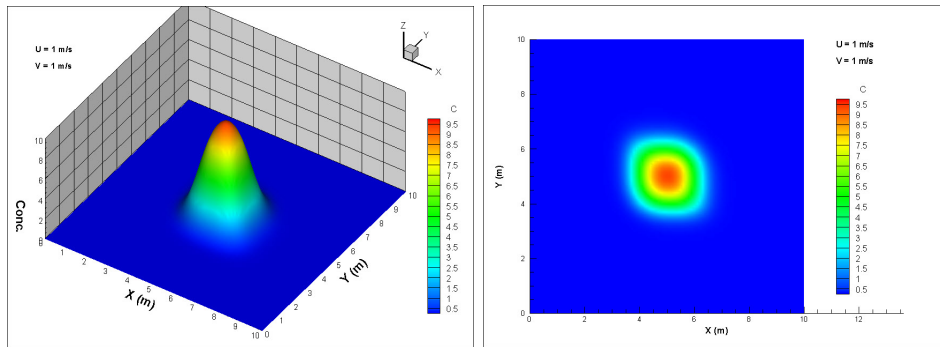Figure 4.8: Numerical results of test 2 at t = 1s

Figure 4.9: Numerical results of test 2 at t = 2s

at t = 1s it is already less than 10 while at t=5s it becomes 9.54. There is negative concentration due to numerical oscillations. However the negative value is quite close to 0 and even hard to be observed because the negative area is so small. The errors are acceptable though getting a little bit bigger as time increases.

4.1.3 Test 2

In test 2, the velocity field in diagonal direction is tested instead of only in x direction, namely U = V = 1.0 m/s. With $\Phi = 0$, the numerical results are shown in the figures 4.8 to 4.12.

Compared with test 1, the numerical dispersion is more obvious and the errors are considerably more significant. As shown in table 4.4, the maximum concentration at t = 5s is only 8.1 and the root mean square error is as high as 0.97. The negative concentration also exists but it is still quite small. The

Figure 4.10: Numerical results of test 2 at t = 3s
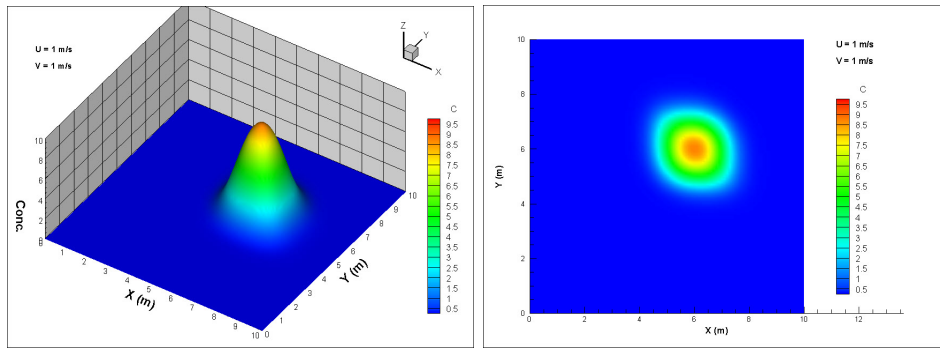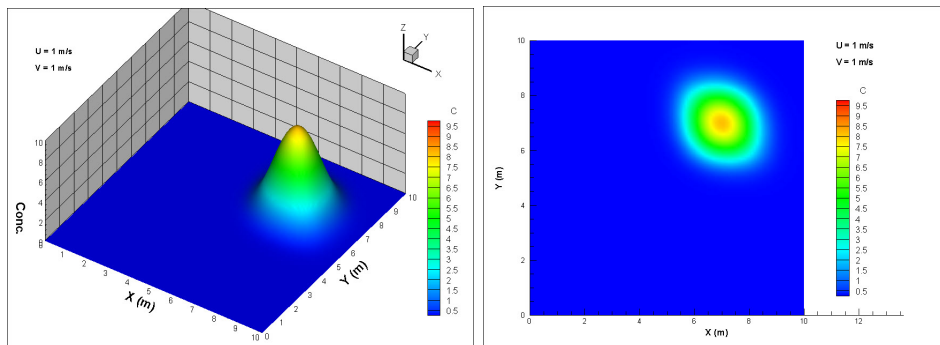

Figure 4.11: Numerical results of test 2 at t = 4s
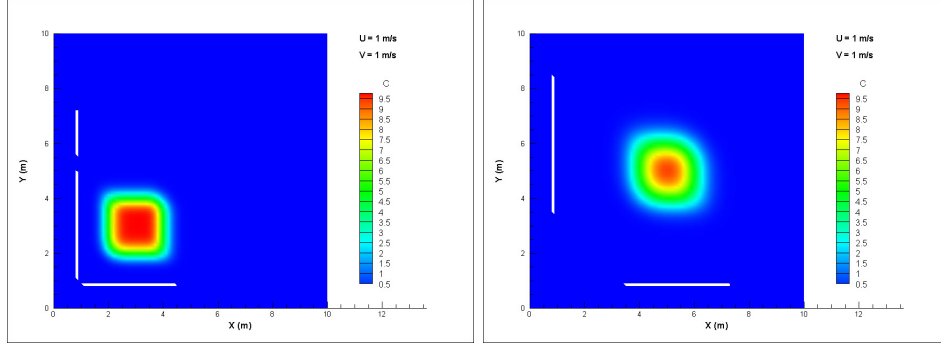

Figure 4.12: Numerical results of test 2 at t = 5s

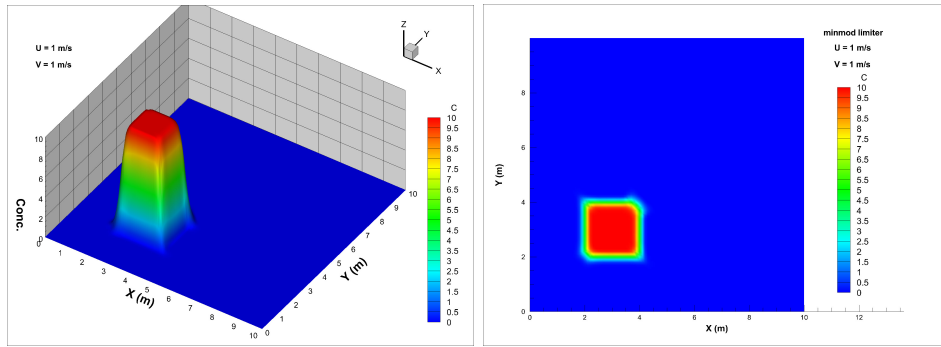Figure 4.13: Distribution of negative area (blank) at t=1s (left) and 3s (right)

Figure 4.14: Numerical results of test 3 at t = 1s

negative area at t = 1s and 3s is shown in figure 4.13.

Table 4.4: The performance of numerical test 2

t(s)	C_{max}	C_{min}	Mean Absolute Error	Root Mean Square Error	Global Mass Relative Error
1	9.99564	-2.69E-21	0.12992	0.57590	1.82E-15
2	9.80101	-2.20E-26	0.19137	0.72958	-8.41E-15
3	9.32428	-1.79E-31	0.23676	0.83048	-3.18E-15
4	8.72305	-1.43E-36	0.27363	0.90884	-2.69E-09
5	8.11311	-1.12E-41	0.30492	0.97462	-7.24E-05

4.1.4   Test 3

In test 3, the effect of minmod limiter will be seen in figures 4.14 to 4.18. The applications of limiters significantly help to regulate numerical dispersion and to produce more satisfactory simulation results.
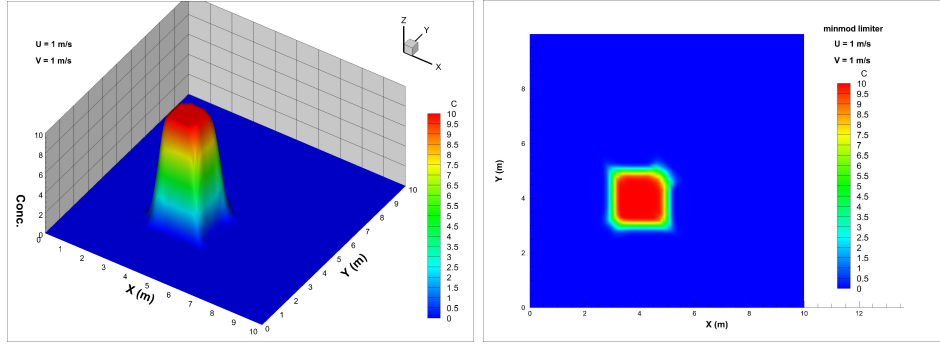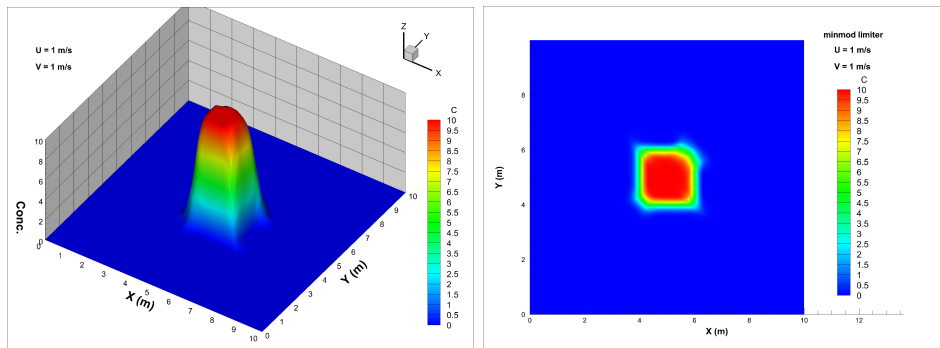
26

Figure 4.15: Numerical results of test 3 at t = 2s
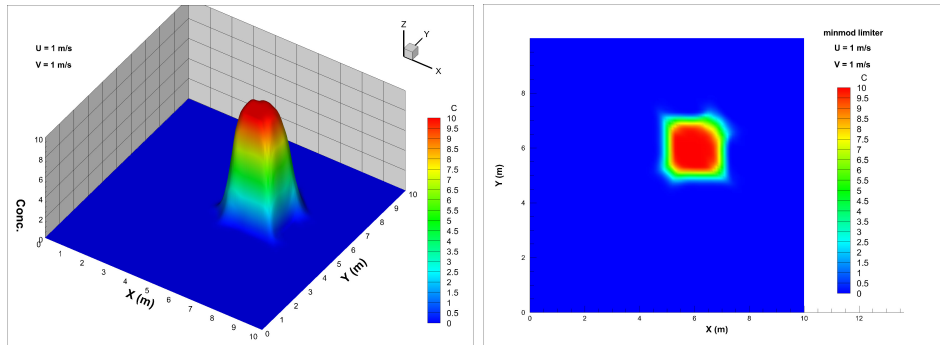

Figure 4.16: Numerical results of test 3 at t = 3s

Figure 4.17: Numerical results of test 3 at t = 4s

Table 4.5: The performance of numerical test 3

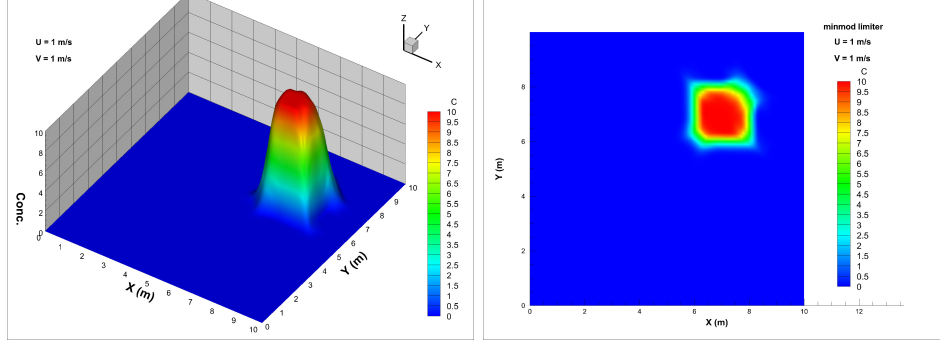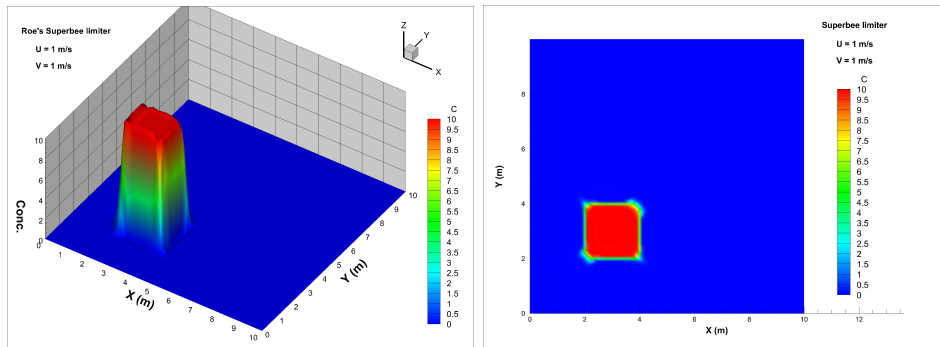| t(s)	C_{max}	C_{min}	Mean Absolute Error	Root Mean Square Error	Global Mass Relative Error
1	10	-1.59E-23	0.04630	0.29696	1.71E-15
2	10	-9.62E-29	0.06500	0.37702	-5.68E-16
3	9.99999	-1.39E-33	0.07912	0.42769	-5.68E-16
4	9.99993	-1.28E-33	0.09114	0.46727	3.98E-15
5	9.99962	-6.91E-34	0.10188	0.50123	3.82E-10

Figure 4.18: Numerical results of test 3 at t = 5s

Figure 4.19: Numerical results of test 4 at t = 1s

As shown in table 4.5 and figure 4.14 to 4.18, the performance of minmod limiter is proven to be good. Though a little bit numerical dispersion still exists, the minmod limiter can limit the reduction of maximum concentration to be in the order of 10^{-4} at t=5s. Also, the errors are much smaller than that in test 2 and the global mass balance is improved.

4.1.5   Test 4

Similarly, the performance of Roe's Superbee limiter ($\beta = 2$) is tested and the results can be found in figures 4.19 to 4.23.

Shown in the figures 4.19 to 4.23 and table 4.6, the Roe's Superbee limiter is found to be overly "anti-diffusive" which was also shown by Anastasiou and Chan ([24]). Obvious ripples can be seen directly from the figures especially at the lower left corner and those ripples seem to be bigger and bigger as time increases. At t = 5s, the maximum concentration is found to be almost
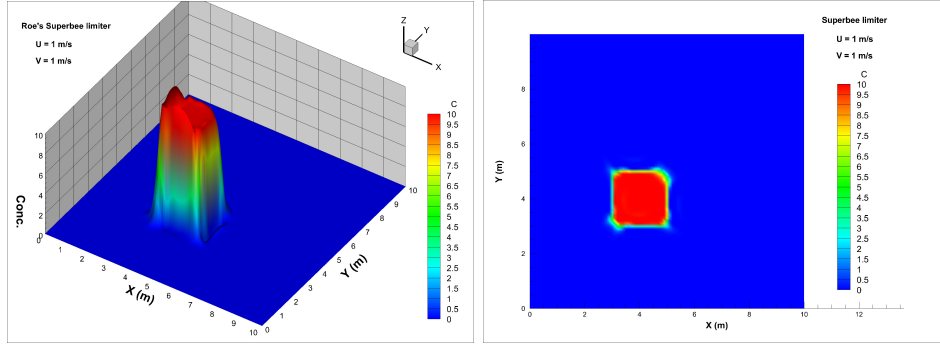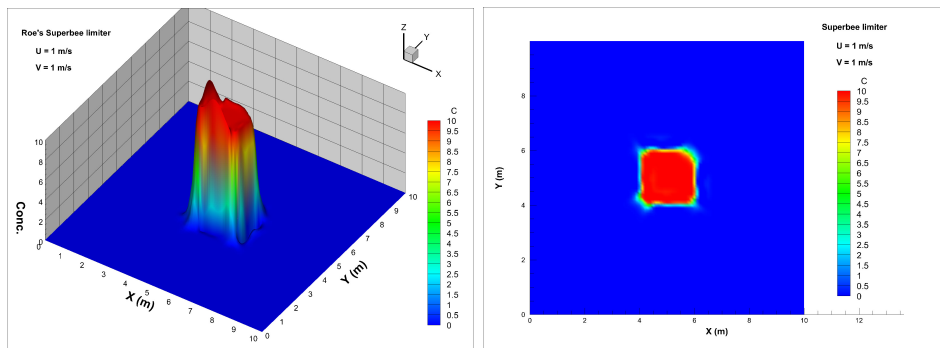
Figure 4.20: Numerical results of test 4 at t = 2s
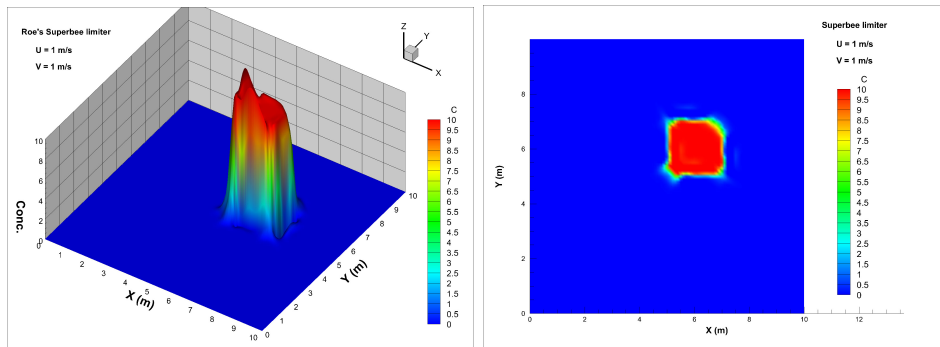

Figure 4.21: Numerical results of test 4 at t = 3s

Figure 4.22: Numerical results of test 4 at t = 4s

Table 4.6: The performance of numerical test 4

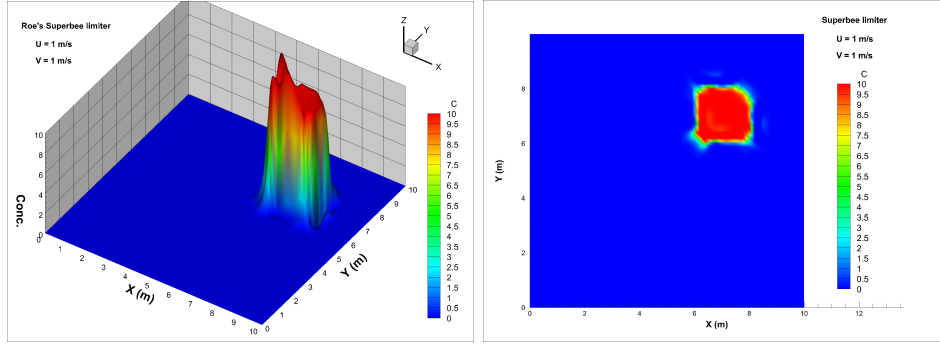| t(s)	C_{max}	C_{min}	Mean Absolute Error	Root Mean Square Error	Global Mass Relative Error
1	10.8492	-8.37E-01	0.02327	0.16417	1.25E-15
2	11.9499	-1.94E+00	0.04099	0.25961	6.82E-16
3	12.8819	-2.91E+00	0.05794	0.35028	-6.82E-16
4	13.5137	-3.64E+00	0.07503	0.43345	2.16E-15
5	13.9594	-4.12E+00	0.08863	0.50317	-1.85E-11

Figure 4.23: Numerical results of test 4 at t = 5s
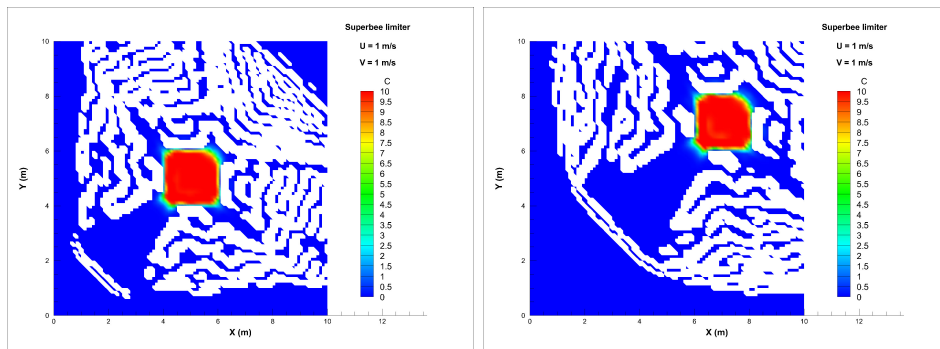

Figure 4.24: The distribution of negative area (blank) at t = 3s (left) and 5s (right)

14 and the minimum is -4.12. The negative area at t = 3s and 5s is shown in figure 4.24. The area is considerably big. However, the global mass balance is still pretty satisfactory and the errors are smaller than minmod limiter. If we only focus on the area where the concentration C is less than -0.001, the blank areas are not that big (see figure 4.25).

4.1.6   Test 5

According to the limiter approach used in the model, the parameter β can be any value between 1 and 2. In order to see how β could affect the numerical result, $\beta = 1.5$ is tried in test 5. The results are shown in figures 4.26 to 4.30.

$\beta = 1.5$ shows the behaviour between minmod and Superbee limiters. It is also overly anti-diffusive but better than Superbee limiter. At t = 5s, the
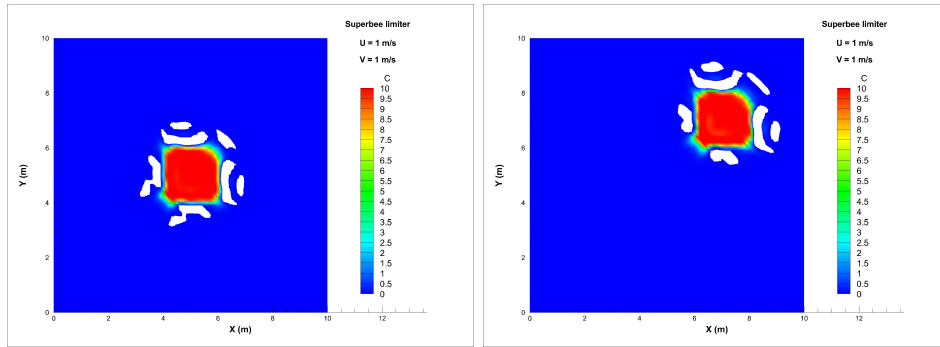
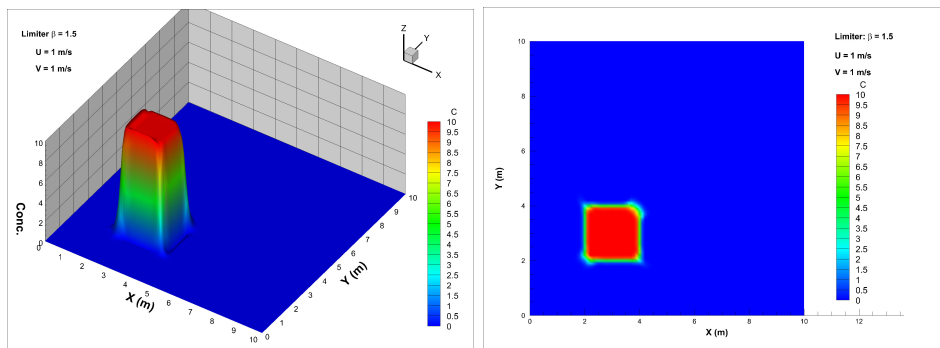Figure 4.25: The distribution of the area where $C < -0.001$ (blank) at t = 3s (left) and 5s (right)

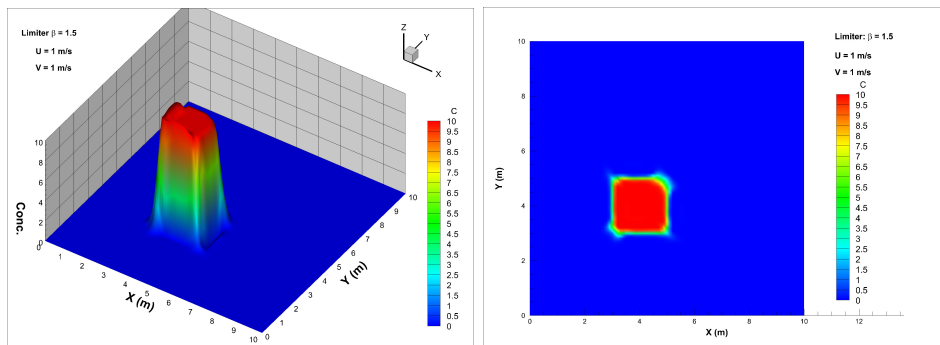

Figure 4.26: Numerical results of test 5 at t = 1s

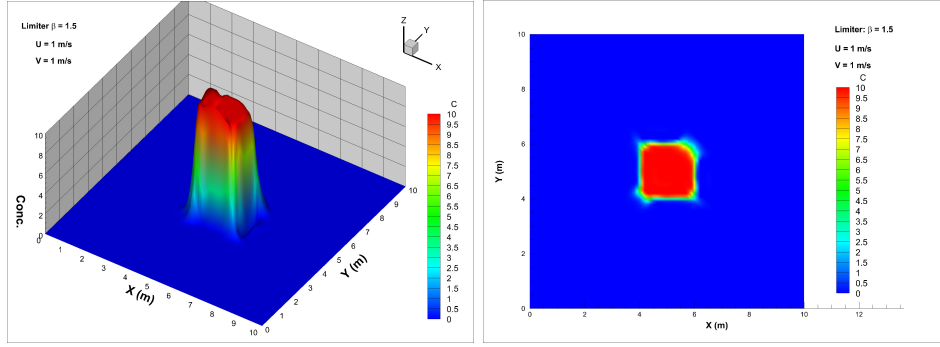

Figure 4.27: Numerical results of test 5 at t = 2s

31

Figure 4.28: Numerical results of test 5 at t = 3s
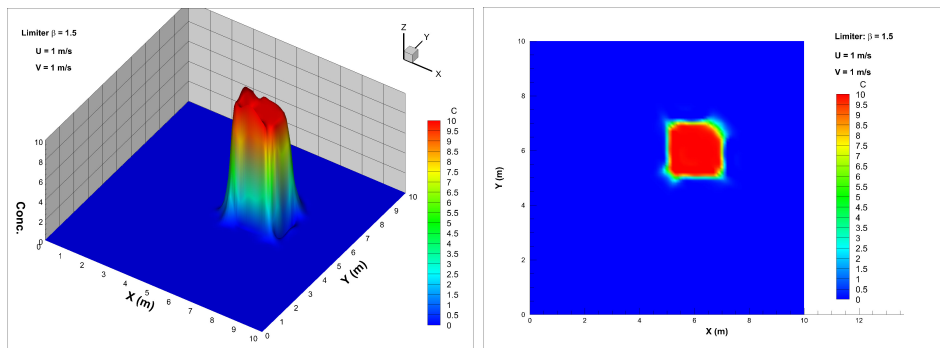
Figure 4.29: Numerical results of test 5 at t = 4s
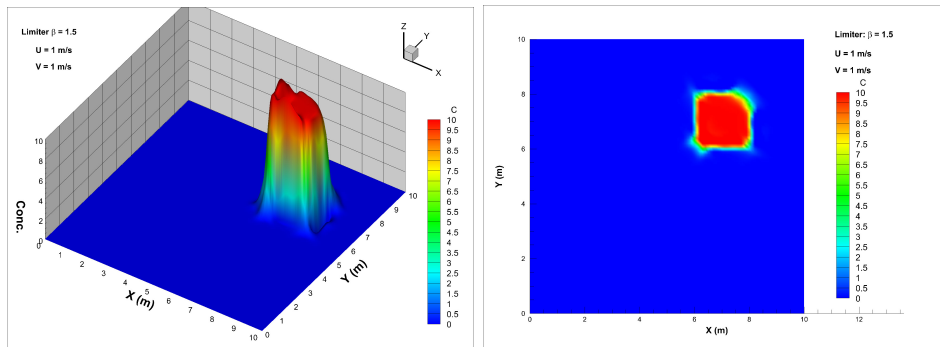
Figure 4.30: Numerical results of test 5 at t = 5s

Table 4.7: The performance of numerical test 5

t(s)	C_{max}	C_{min}	Mean Absolute Error	Root Mean Square Error	Global Mass Relative Error
1	10.4874	-4.87E-01	0.02495	0.16720	1.59E-15
2	10.9785	-9.67E-01	0.03620	0.22683	-2.73E-15
3	11.436	-1.39E+00	0.04738	0.27875	0.00E+00
4	11.7765	-1.68E+00	0.05704	0.32449	4.55E-16
5	12.0367	-1.89E+00	0.06684	0.37004	2.74E-11

maximum concentration is around 12, smaller than the one in test 4 (around 14). Also, the ripples develop mostly at lower left corner. The minimum concentrations is not as small as those in test 4. The comparison between test 2, 3, 4 and 5 at t = 5s is shown in table 4.8.

Table 4.8: Comparison among test 2 - 5 at t = 5s

Test	C_{max}	C_{min}	Mean Absolute Error	Root Mean Square Error	Global Mass Relative Error
$\Phi=0$	8.11311	-1.120E-41	0.30492	0.97462	-7.2400E-05
minmod	9.99962	-6.910E-34	0.10188	0.50123	3.8200E-10
Superbee	13.95940	-4.120E+00	0.08863	0.50317	-1.8500E-11
$\beta=1.5$	12.03670	-1.895E+00	0.06684	0.37004	2.7383E-11

Shown in the comparison, the optimal scheme could possibly be achieved by adjusting the value of β. It probably should be between 1 and 1.5. However more tests need to be run before making any decision because the relationship is probably not linear.

4.1.7 Summary

Those pure advection tests show that the numerical calculation of 2D advection equation has been correctly implemented in the model with the application of limiter approaches, which can improve simulation accuracy and alleviate numerical dispersion. In the case of diagonal velocities, the numerical errors may be bigger than the ones in the case of unidirectional velocity. The upwind scheme has a relatively big problem of numerical diffusion. The limiters do help a lot to improve the results and offer higher accuracy. It is shown that Roe's Superbee limiter is overly anti-diffusive under this condition and an optimal limiter may be achieved by adjusting the value of β which need to be further proved by more tests.

Overall, the numerical results show that the model is verified in those test cases. Moreover, they help us understand the behaviours of the different limiters. However, one should note that those cases only test the advection part of the 2D advection-diffusion equation without considering the diffusion part. The velocities are taken as constant so that the transport module is actually not coupled with the flow module in those tests. Although the numerical methods used herein have no trouble to deal with unstructured meshes, regular triangular mesh is used in order to conveniently compare the numerical results with the analytical solution. Therefore, after those pure

advection tests, it can be good to further test the model in a real-world project.

4.2 Dye Tracer Study in the Chicago River

To verify the model's applicability to real world problems, the model is applied to simulate a dye tracer study, which was done in the Chicago River by USGS in December 2009. The numerical results are compared with the field measurement data got by USGS. Also, the study could help to identify possible problems which may not be revealed by simply pure advection tests, for example, the link between hydrodynamic results and transport module.

4.2.1 Background

The Chicago River flows through the downtown of Chicago which is the third largest city in U.S.. The river used to flow into the Lake Michigan. In 1900, people built the Chicago Sanitary and Ship Canal and artificially made the water flow away from the Lake Michigan, in order to protect the water supply for the city of Chicago.

Recently, people in the United States paid much attention to the threat of some alien species, Asian Carps. Asian carp is a general term including silver carp (Hypophthalmichthys molitrix), bighead carp (H. nobilis), black carp (Mylopharyngodon piceus) and grass carp (Ctenopharyngodon idella), which are all native to Asian countries and were introduced into U.S. about 30 years ago. Bighead and silver carp were first introduced to Arkansas in 1972 with the purpose of improving water quality. Asian carps feed on plankton so they were good for the control of algae blooms. However, the problem of biological invasion of Asian carps were put forward in recent years because of their tremendous advantageous biological characteristics, such as powerful environmental suitability and high growth rate ([25]), and the lack of natural enemies in U.S. The establishment of Asian carps badly threatened native species and can potentially cause ecological harm by changing the aquatic environment. The researchers have found that the distribution of Asian Carps is expanding and approaching to the Great Lakes. It is believed that once the Asian Carps reach the Great Lakes, it will be possible
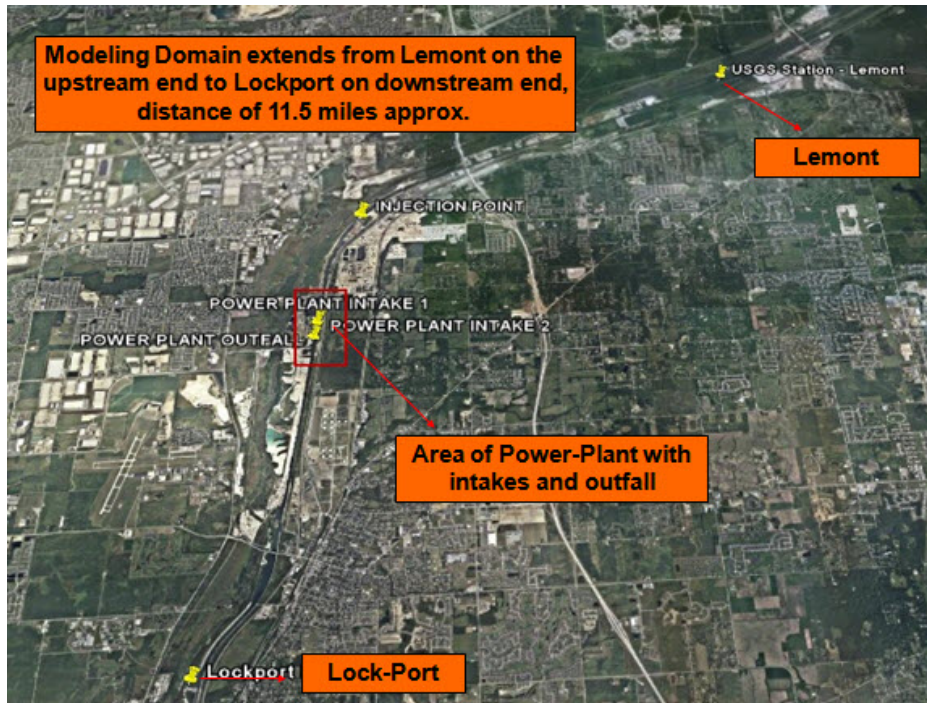
Figure 4.31: Study area of the dye tracer study simulation

for them to go almost everywhere in the United States through the waterways connected to the Great Lakes. Many researches and action have been conducted including the fish kill operation in the Chicago River by using piscicide Rotenone. Before injecting piscicide, a dye tracer study was done by the USGS in December 2009, using Rhodamine, in the zone of the river, where piscicide will be injected, so that the dispersal and other important environmental characteristics of the river can be studied. The study domain of the river was the south branch of the Chicago River, from Lemont Street upstream to Lockport downstream (see figure 4.31).

4.2.2 Some Basic Information

The total length of the river in the study domain is around 11.5 miles. The topography data of this study domain was got from field measurement and provided by USGS (see figure 4.32). The upstream discharge and water height data can be found from USGS Lemont Station. The discharge data is used as upstream boundary condition (see figure 4.33). The water height data is used to do model validation. The downstream end of the study
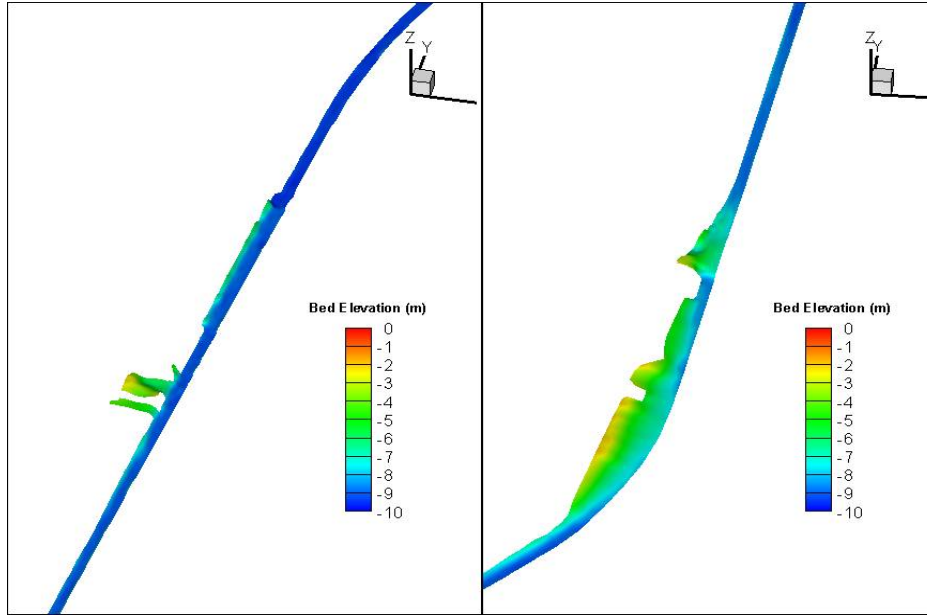
35

Figure 4.32: Topography data of the study area

domain is the Lockport Powerhouse. Unfortunately, there is no continuous measurement or any station there, but the flow discharge was estimated according to some field measurement data during the same period (see figure 4.34).

During this study, the Rhodamine dye was injected into the river with the discharge of 177.3 ml/min and the concentration of the dye at the injection point was 2.3E8 ppb. The injection duration is 9 hours, from 19:51 Dec. 2nd to 04:47 Dec. 3rd in 2009 (see figure 4.35).

It is worthy mentioning that the depth of the river is around 9m, while the width is around 70m. The dye is easily mixed in the vertical direction. Thus a 2D depth-averaged model is applicable in this study. Another noticeable issue about this domain is that there is a power plant along the river which takes the water from the river for the cooling purpose. The power plant intake and outfall are shown in the figure 4.36. Compared with the length of the study domain, the distance between intake and outfall is quite small. The power plant may help enhance the mixing in the transverse direction of the river. However, because the river is not too wide, the observation shows that the dye was well mixed quickly and easily in the transverse direction after injection. Therefore, the power plant does not affect too much in this dye tracer study, especially in the areas far away from the power plant.
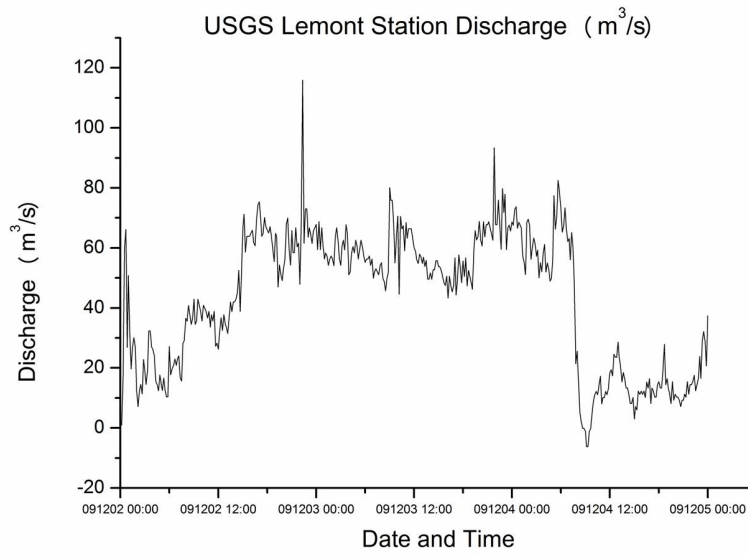
36

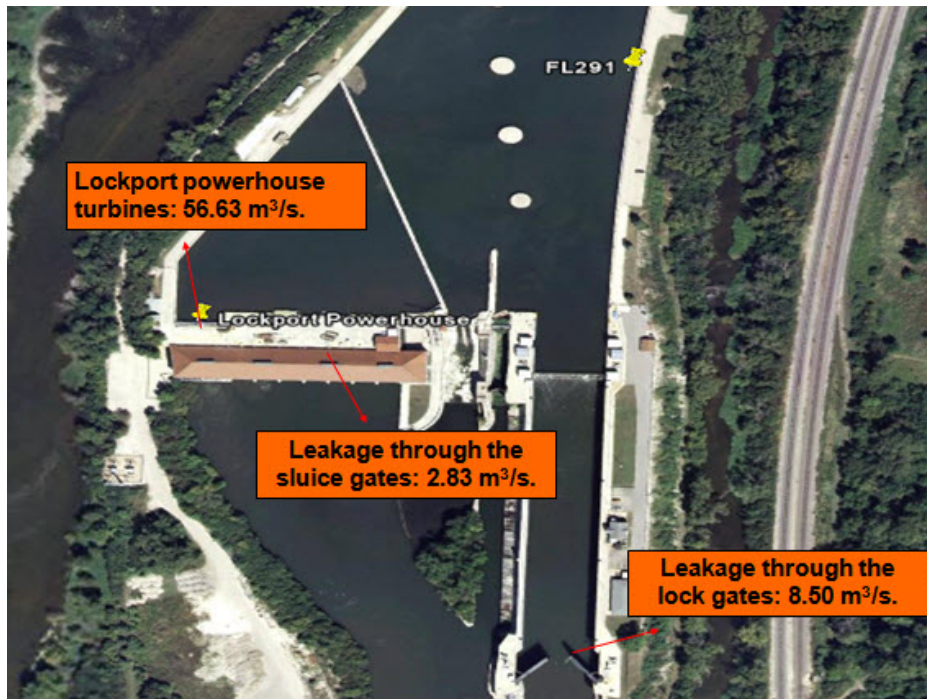Figure 4.33: Upstream discharge data from USGS Lemont Station

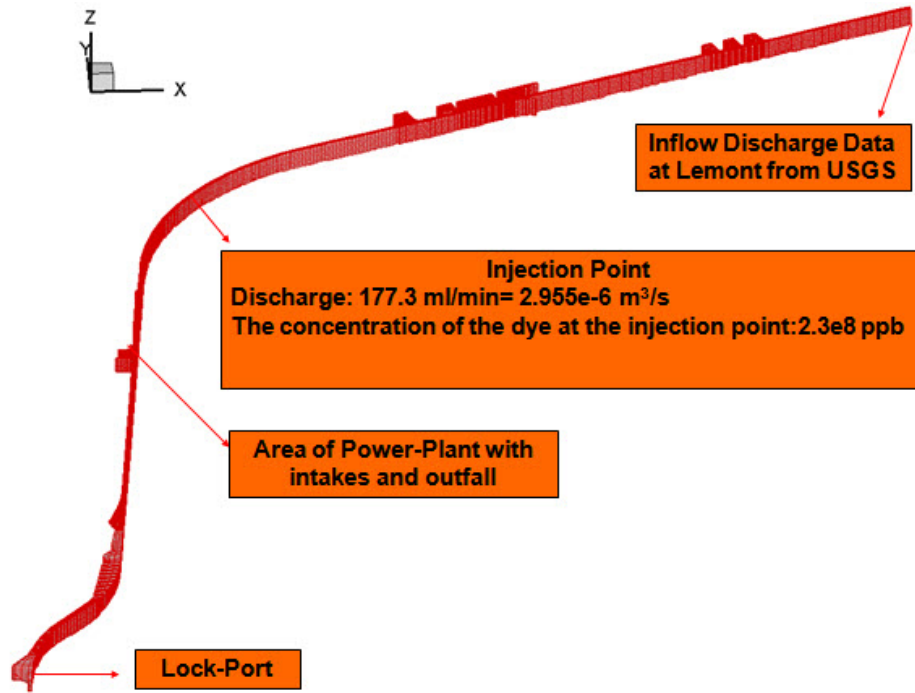Figure 4.34: Downstream discharge at the Lockport Powerhouse

Figure 4.35: The location and other information of the dye injection

Figure 4.36: Power plant in the study domain
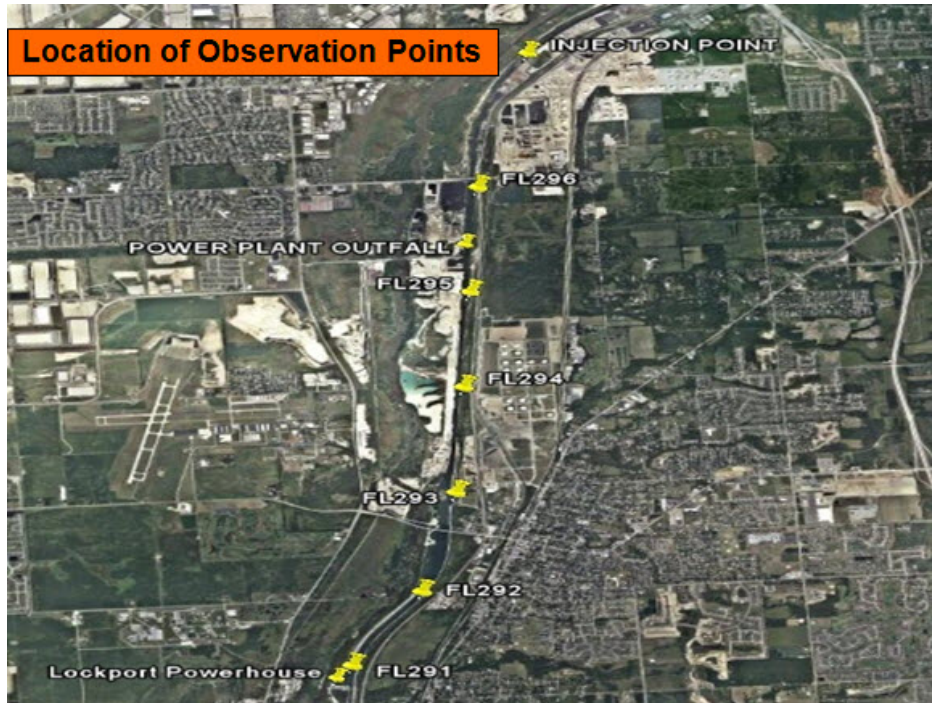
Figure 4.37: Location of observation points

In the field study, USGS set up fluorometer at 6 different points in the domain as shown in figure 4.37, and recorded the evolution of dye with time.

4.2.3 Model Settings

Mesh Generation

The triangular meshes were generated by using the software GAMBIT (see figure 4.38). The size of the triangular edges was around 20 m. There were totally 7974 cells and 5057 nodes.

Boundary Conditions

The discharge data (figure 4.33) at upstream inlet was taken as upstream boundary condition. The previous HydroSed model can only use constant discharge or water height as boundary conditions. The new model is able to handle changing boundary conditions which mean upstream boundary condition (e.g. inflow rate) and downstream boundary condition (e.g. water

39

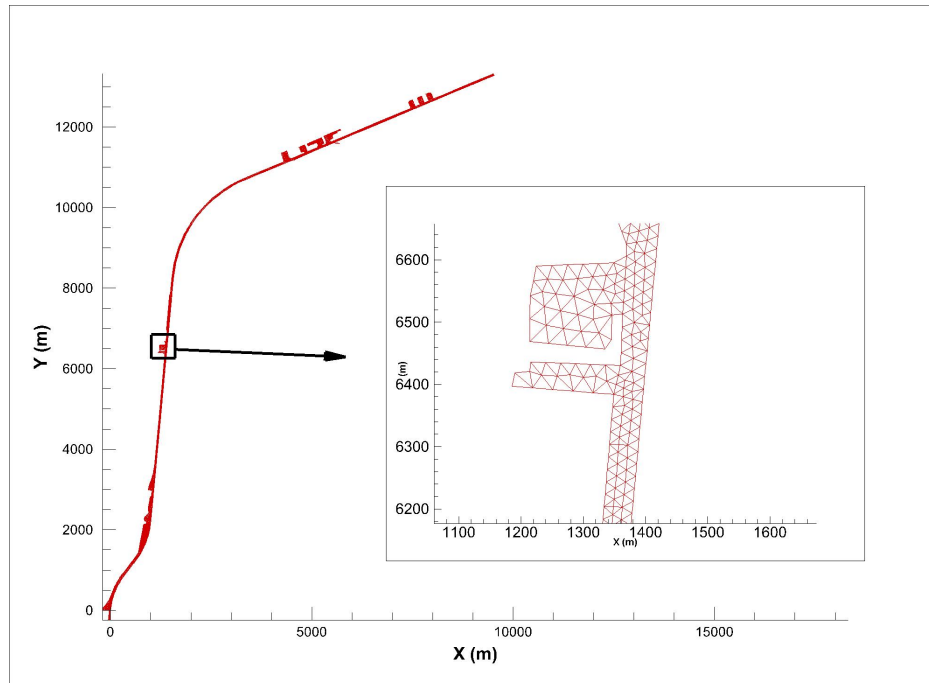Figure 4.38: Unstructured meshes for the study in Chicago River (7974 cells and 5057 nodes)

surface elevation) can vary with time. The upstream discharge data can be input through the input file "qt.txt", and the downstream water surface elevation data may be input by using "ht.txt". The format of those files and more details can be found in the user's manual in the Appendix.

The lack of downstream measurement data did result in some troubles for specifying downstream boundary condition. Fortunately, the slope of the river in this study is quite small and the bed is generally flat except some side-slip structures (see figure 4.32). Many numerical tests showed that the water surface elevation in the whole domain was basically the same at the same time. In July 2010, USGS set up another temporary station near Lockport (USGS 05536998 CHICAGO SS CANAL AT LOCKPORT CONTROLLING WORKS, IL). The comparison of water surface elevation between that station and Lemont station during the period of July 4 - September 7, 2010 also showed that the water surface elevation was very close. Therefore, a simplified sketch of the upstream water height data was used as downstream boundary condition (see figure 4.39). Furthermore, the numerical results of upstream water surface elevation was validated later.
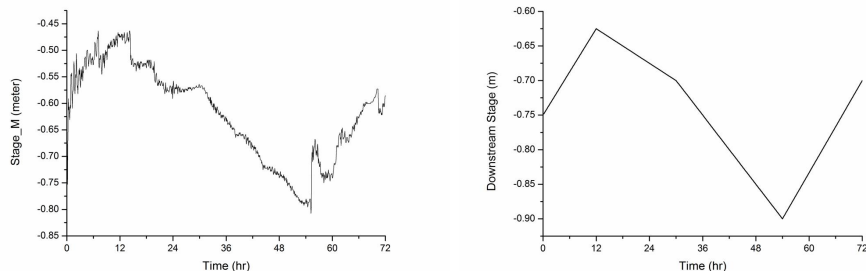
40

Figure 4.39: Downstream boundary condition

The injection of dye was read into the model by using the file "ct.txt" where the location of injection and injection rate varying with time were specified (see Appendix for more details). As discussed above, the power plant was not considered in the model. Two methods were used to deal with the dispersion coefficients: specifying them as constant and using the formulas (see equation (2.45)).

4.2.4 Brief Introduction to EFDC model

In order to better evaluate the performance of the new 2D HydroSed model, it is useful to use another widely used 3D numerical model in the same project and compare the results. The Environmental Fluid Dynamics Code (EFDC) is chosen to perform that task. The EFDC model was developed at the Virginia Institute of Marine Science (Hamrick, 1992 [26]), which is a public domain code maintained by Tetra Tech, Inc. with the supported of US EPA. It has the modules of hydrodynamics model, eutrophication model and sediment contaminant transport model. The model has been widely used over the world in environmental fluid studies (Sinha et al. 2010 [27]; Liu and Garcia, 2008 [28]; Ji et al., 2007 [29]; Jiang and Shen, 2009 [30]) and river morphodynamics studies (Kong et al. 2009 [31]).

The model uses a curvilinear-orthogonal horizontal grid and a sigma vertical grid. In hydrodynamics part, it solves the three-dimensional free surface flow equations for continuity, momentum, salinity and temperature. The governing equations are as follow.

$$\frac{\partial \left(mHu \right)}{\partial t} + \frac{\partial \left(m_y Huu \right)}{\partial x} + \frac{\partial \left(m_x Huv \right)}{\partial y} + \frac{\partial \left(muw \right)}{\partial z} -$$
$$\left(mf + v\frac{\partial m_y}{\partial x} - u\frac{\partial m_x}{\partial y} \right) Hv = -m_y H\frac{\partial \left(g\varsigma + p \right)}{\partial x} - \qquad (4.6)$$
$$m_y \left(\frac{\partial h}{\partial x} - z\frac{\partial H}{\partial x} \right) \frac{\partial p}{\partial z} + \frac{\partial}{\partial z}\left(mH^{-1}A_v\frac{\partial u}{\partial z} \right) + Q_u$$

$$\frac{\partial \left(mHv \right)}{\partial t} + \frac{\partial \left(m_y Huv \right)}{\partial x} + \frac{\partial \left(m_x Hvv \right)}{\partial y} + \frac{\partial \left(mvw \right)}{\partial z} -$$
$$\left(mf + v\frac{\partial m_y}{\partial x} - u\frac{\partial m_x}{\partial y} \right) Hu = -m_x H\frac{\partial \left(g\varsigma + p \right)}{\partial y} - \qquad (4.7)$$
$$m_x \left(\frac{\partial h}{\partial y} - z\frac{\partial H}{\partial y} \right) \frac{\partial p}{\partial z} + \frac{\partial}{\partial z}\left(mH^{-1}A_v\frac{\partial v}{\partial z} \right) + Q_v$$

$$\frac{\partial p}{\partial z} = -gH\frac{\rho - \rho_0}{\rho_0} \qquad (4.8)$$

$$\frac{\partial \left(m\varsigma \right)}{\partial t} + \frac{\partial \left(m_y Hu \right)}{\partial x} + \frac{\partial \left(m_x Hv \right)}{\partial y} + \frac{\partial \left(mw \right)}{\partial z} = 0 \qquad (4.9)$$

$$\frac{\partial \left(m\varsigma \right)}{\partial t} + \frac{\partial \left(m_y H\int_0^1 udz \right)}{\partial x} + \frac{\partial \left(m_x H\int_0^1 vdz \right)}{\partial y} = 0 \qquad (4.10)$$

$$\rho = \rho\left(S, T \right) \qquad (4.11)$$

$$\frac{\partial \left(mHS \right)}{\partial t} + \frac{\partial \left(m_y HuS \right)}{\partial x} + \frac{\partial \left(m_x HvS \right)}{\partial y} + \frac{\partial \left(mwS \right)}{\partial z} =$$
$$\frac{\partial}{\partial z}\left(mH^{-1}A_b\frac{\partial S}{\partial z} \right) + Q_S \qquad (4.12)$$

$$\frac{\partial \left(mHT \right)}{\partial t} + \frac{\partial \left(m_y HuT \right)}{\partial x} + \frac{\partial \left(m_x HvT \right)}{\partial y} + \frac{\partial \left(mwT \right)}{\partial z} =$$
$$\frac{\partial}{\partial z}\left(mH^{-1}A_b\frac{\partial T}{\partial z} \right) + Q_T \qquad (4.13)$$

where m_x and m_y are the square roots of the diagonal components of the metric tensor; m = $m_x m_y$; u and v are the horizontal velocities in the curvilinear orthogonal coordinates x and y; w is the dimensionless velocity in coordinate z; H is total water depth which equals the sum of h (depth below the undisturbed free surface) and ζ (surface elevation); p is the amount of physical pressure in excess of the reference density hydrostatic pressure normalized by the reference density ρ_0; f is the Coriolis parameter; A_v is the vertical turbulent viscosity; Q_u and Q_v are momentum source and sink terms modelled by subgrid-scale horizontal diffusion; S and T represents salinity and temperature respectively; Q_S and Q_T are the source and sink terms for salinity and temperature respectively; A_b is vertical turbulent diffusivity. A_v and A_b are computed by second moment turbulent model developed by Mellor and Yamada ([32]) and modified by Galperin et al. ([33]). For the computation of contaminant transport, the advection-diffusion equation which is similar to equation (4.12) and (4.13). The details about numerical schemes used in EFDC can be found in reference [26].

The mesh was generated by using the software Gridgen. There were totally 8111 horizontal cells, which is similar with the number of horizontal cells in HydroSed simulation, and 8 vertical layers in the mesh (see figure 4.40). It is notable that EFDC uses curvilinear-orthogonal meshes in horizontal directions. Due to this orthogonal requirement, fitting computational mesh smoothly to real boundaries is quite challenging and the orthogonal quality of meshes is very important, while the unstructured meshing techniques used in HydroSed model offers an advantage in generating grids for complex topographies compared to structured ones. The power plant was considered in the simulation. The settings of boundary conditions were the same as the ones used in HydroSed simulation. The numerical results are shown together with the results got in HydroSed model in the following section.

4.2.5   Numerical Results

Validation of Upstream Water Surface Elevation

It became important to check how the hydrodynamics simulation was because of the assumption we made for downstream boundary condition. The
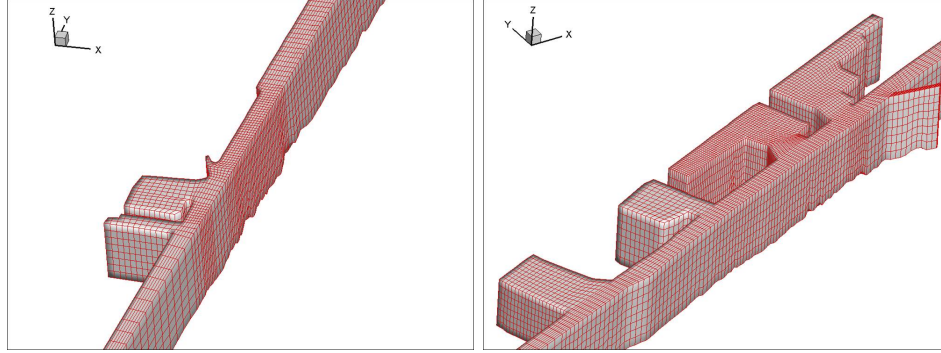
Figure 4.40: Computation mesh for EFDC simulation

comparison between field measurement data, EFDC simulation result and HydroSed simulation result is shown in figure 4.41. Generally both of the simulation results match the measurement data well, which on the other hand verifies the assumption made before. As far as water surface elevation is concerned, the performance of HydroSed is as good as that of EFDC, which further proves that the employment of varying boundary conditions is fine. The error is shown in figure 4.42. The mean absolute error is around 0.04m which is acceptable.

Dye Concentration Results

As mentioned above, the numerical results of the evolution of the dye concentration was compared with the field measurement at six locations (see figure 4.37). The comparison is shown in figures 4.43 to 4.48. There are two series of HydroSed results in the figures. The series of "HydroSed2D result" correspond to the numerical results by using constant dispersion coefficients. Although one can find recommended ranges from Fischer et al. [34], many different constants need to be tried in order to find the ones which worked best. However, it was very time consuming and impractical in the real-world projects which require prediction. On the other hand, the series of "HydroSed2D_formula result" show the numerical results by using formula (2.45). It is shown that the formula works very well in this study. It gives better performance than constant coefficients in downstream location 291 and 292. However, it must be mentioned that the formula needs more check since this dye tracer study is an advection dominated problem and the
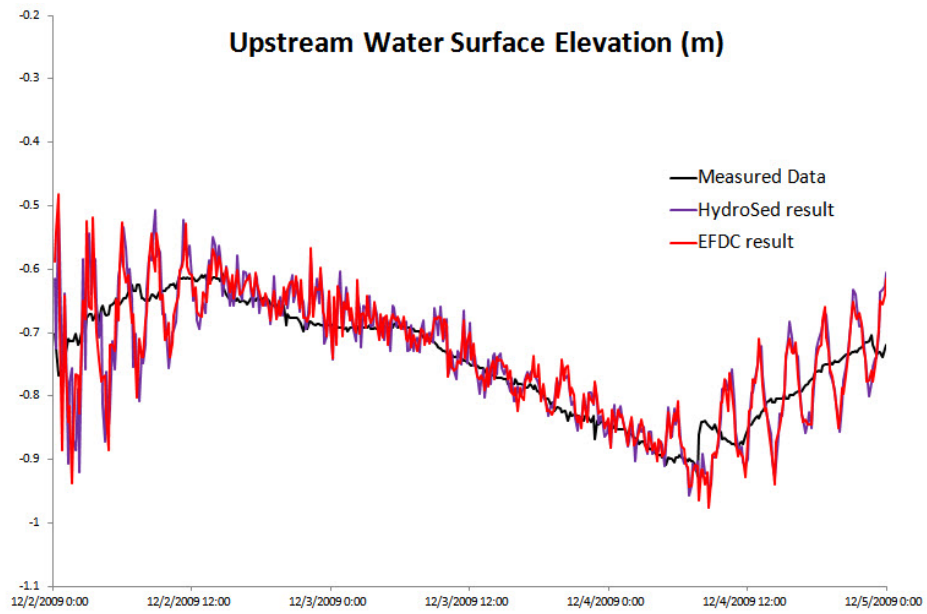
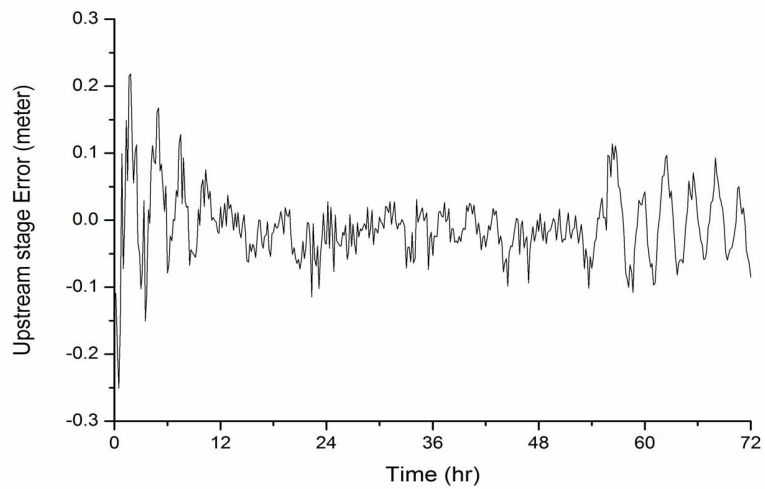Figure 4.41: Comparison of upstream water surface elevation
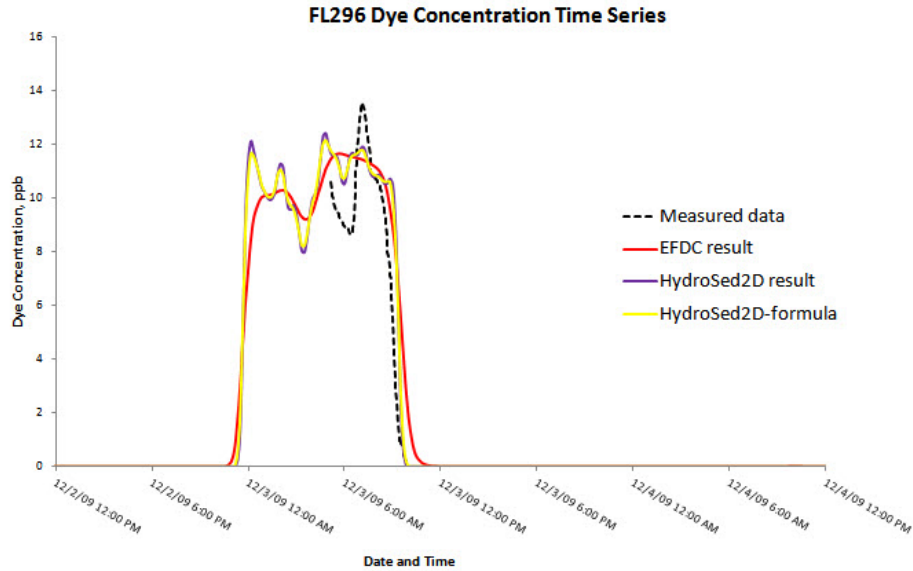

Figure 4.42: Error Analysis

45

Figure 4.43: The evolution of dye concentration at location 296

dispersion coefficients are relatively small.

4.2.6 Summary

The study of the Chicago River further verified the model. The contaminant transport equation was solved with the water flow equations. Irregular triangular meshes were used. It was a good test for varying boundary conditions and the formulas for calculating dispersion coefficients. A widely used 3D model EFDC was conducted together with the HydroSed model in order to better evaluate the performance of the HydroSed model. Basically speaking, the transport module in the new HydroSed model works very well.
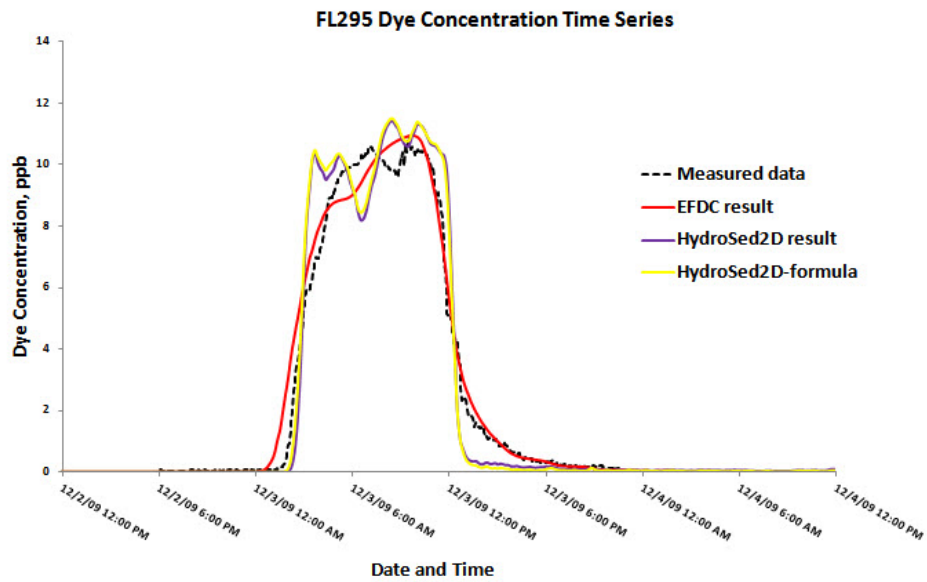
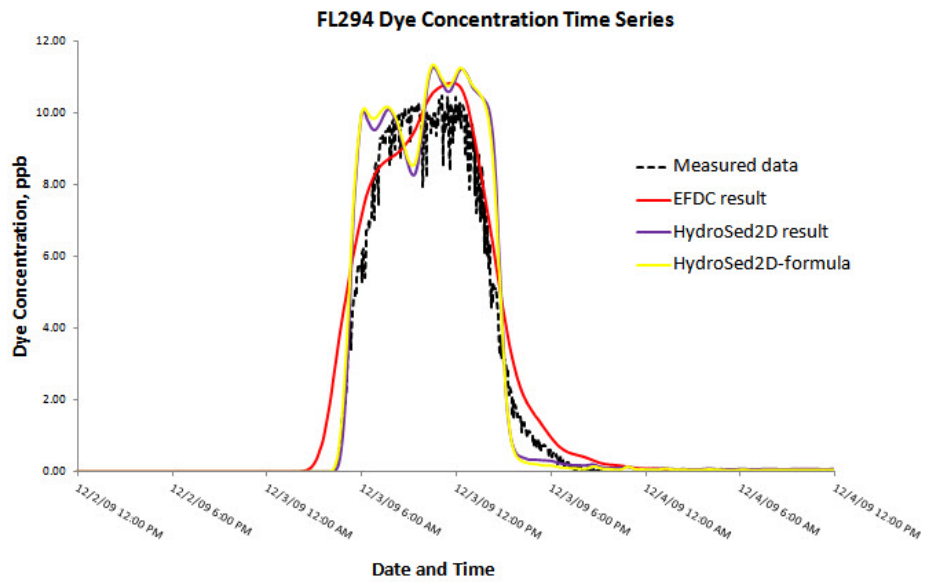Figure 4.44: The evolution of dye concentration at location 295

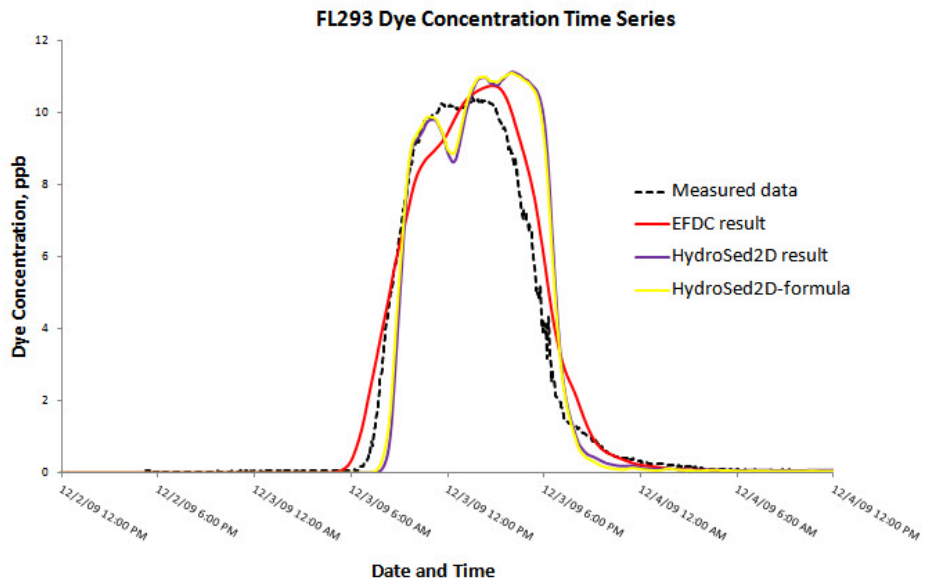Figure 4.45: The evolution of dye concentration at location 294

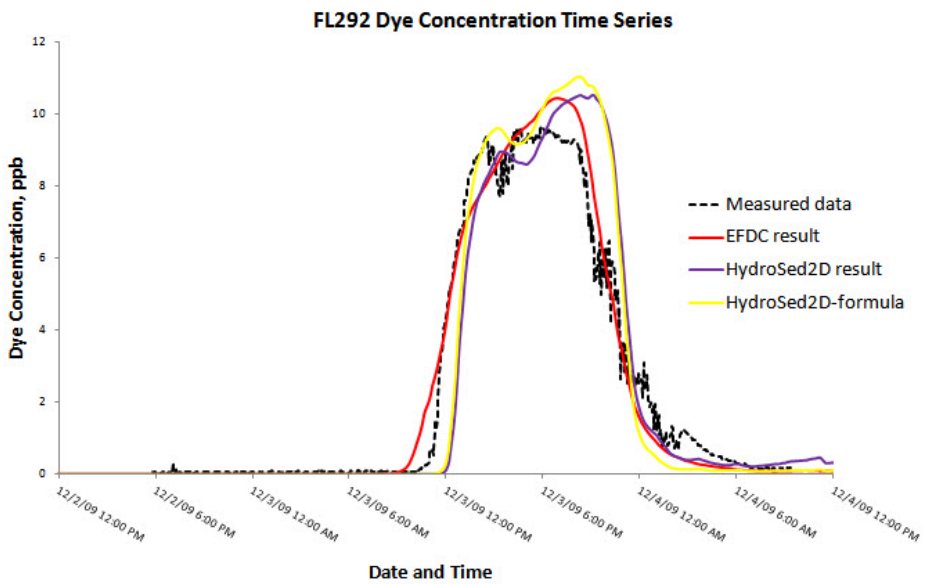Figure 4.46: The evolution of dye concentration at location 293

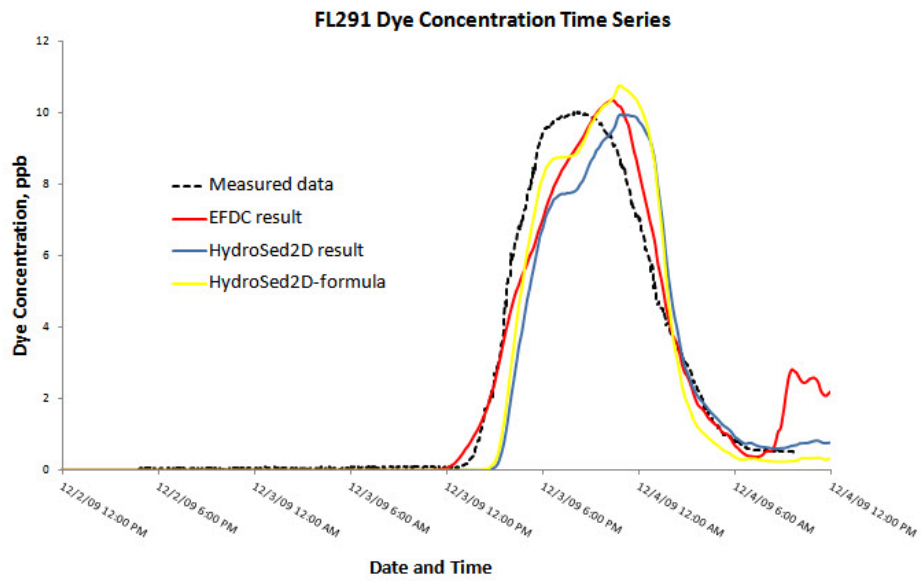Figure 4.47: The evolution of dye concentration at location 292

Figure 4.48: The evolution of dye concentration at location 291

CHAPTER 5

MODEL APPLICATION

5.1 Background

In this chapter, the modified HydroSed model was used to study the potential impacts of planned hydraulic structures in the Guayas watershed, Ecuador (see figure 5.1). The Guayas watershed is a key region for economic development in Ecuador because of abundant aquatic product in this area. However, due to seasonality of the rain distribution, its production capacity has been adversely affected by the problems related with flooding, sediment transport and inefficient natural drainage. In order to overcome those problems, a series of hydraulic projects are planned to be built in the southeast of the Guayas watershed including three sub basins, the Bulubulu River, the Cañar River and the Naranjal River with a total extension of around 5,000 km^2. This study focused on one of those projects, a diversion dam located in the Cañar River. The sluice gates are going to set across the existing river. On the other hand, spillway is designed followed by man-made channels for separated water to flow into another areas. The hydraulic structures aim at diverting a portion of the flow of Cañar River from its natural course so that the flood control ability in downstream region can be improved. The potential impacts of this diversion dam should be carefully studied, especially the issue of sedimentation process.

The Cañar River has three tributaries: Patul, Piedras and Norcay Rivers. The domain of interest is approximately 38 km long. In figure 5.2, the bathymetry information in the whole domain is given. Upstream of the domain is situated in a mountainous area therefore the bed elevation changes quite dramatically over the first 10-15 km of the domain. The maximum expected flow discharge in Cañar River is estimated to be around 1700 m^3/s. Due to variation of rainfall distribution over the year, the region experiences
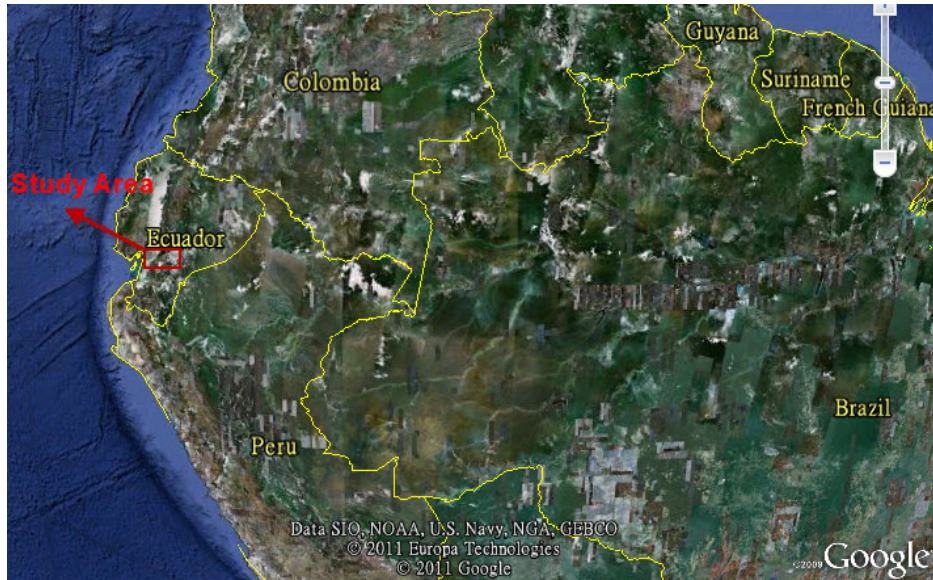
Figure 5.1: The location of study area

flooding events frequently. The natural drainage is poor in the watershed and furthermore, Cañar River is observed to have high sediment transport capacity. The local authorities have carried out geological and geotechnical surveys and designed the diversion dam to be built in the area, which aims to reduce the discharges in Cañar River in high flow seasons. The anticipated location of the planned structure is shown in figure 5.2.

For the purpose of design, a 1D hydrodynamics model using the HEC-RAS model was developed by the research and academic unit PROMAS (Soil and Water Management Program) at the University of Cuenca-Ecuador. HEC-RAS (River Analysis System) is a standard riverine 1D numerical model that solves the full 1D St. Venant equations for unsteady open channel flow ([35]). This model was developed by the United States Army Corps of Engineers and is considered to be one of the most widely used floodplain hydraulics models in the world ([36]).

However, even though a detailed topographical survey of the area is provided, unfortunately field data in terms of water surface elevation, flow discharges and velocities are found lacking. With this limitation, the numerical model can hardly be calibrated and validated. Moreover, the 1D model cannot capture the effects of complex bank and bed geometry. Although 1D HEC-RAS model can be used to estimate sediment transport, the limitations are obvious due to its one-dimensional assumptions and lack of considering
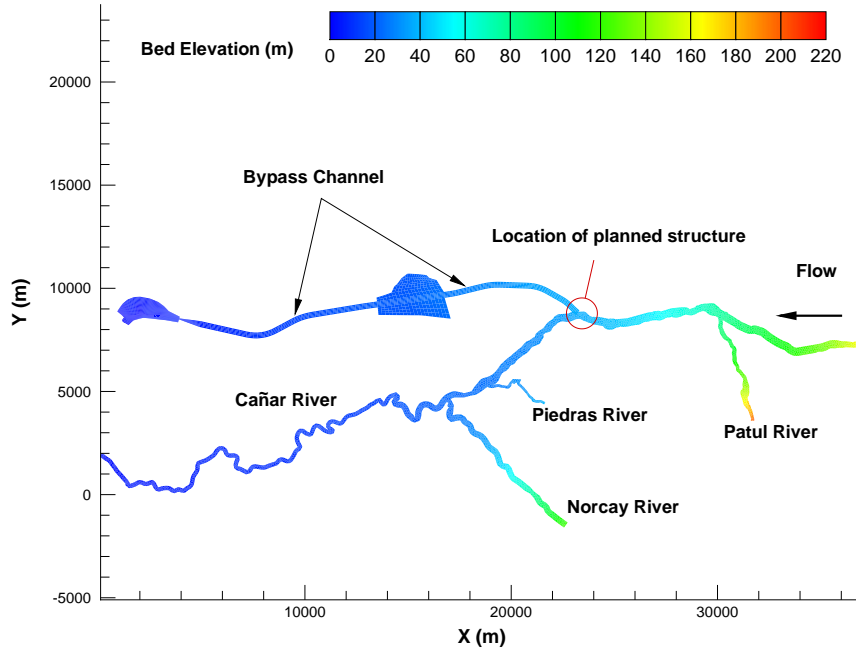
Figure 5.2: Bed elevation information in the research domain

river morphodynamics. Therefore, it is necessary to use some other higher
dimensional numerical models so that results got by different models can be
compared and checked reciprocally which can surely make researchers more
confident. The author and his colleagues applied the HydroSed model and
other two 3D models (EFDC, FLUENT) in this study. The specific study
area of each model can be seen in figure 5.3.

The new HydroSed model was used to evaluate hydrodynamics and sed-
iment transport in two areas: one is the downstream domain very close to
planned hydraulic structures; the other one is the bypass channel where the
water drained from the Cañar River flows (see figure 5.4).

5.2 Numerical Results of Case 1

In order to see the impact of hydraulic structures more clearly, a short reach
of the river downstream of the planned location of hydraulic structures was
selected as the simulation domain by using the HydroSed2D model (see figure
5.3). As shown in figure 5.5, triangular elements were used as computational

52

Figure 5.3: The specific study area of different numerical models

Figure 5.4: Original bed elevation in drainage areas

53

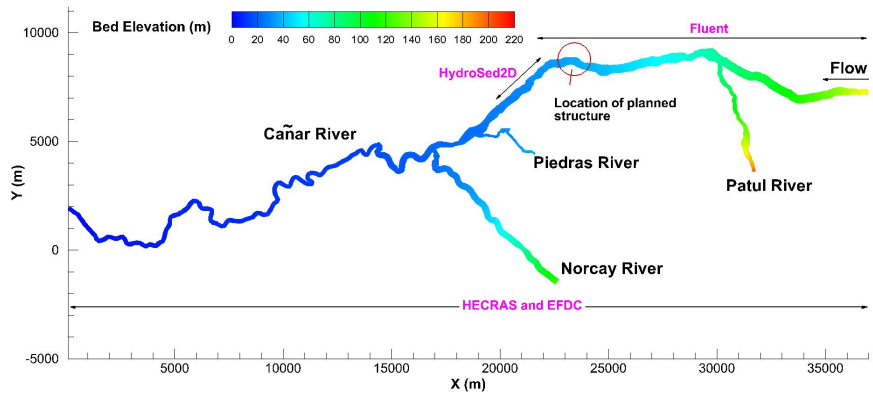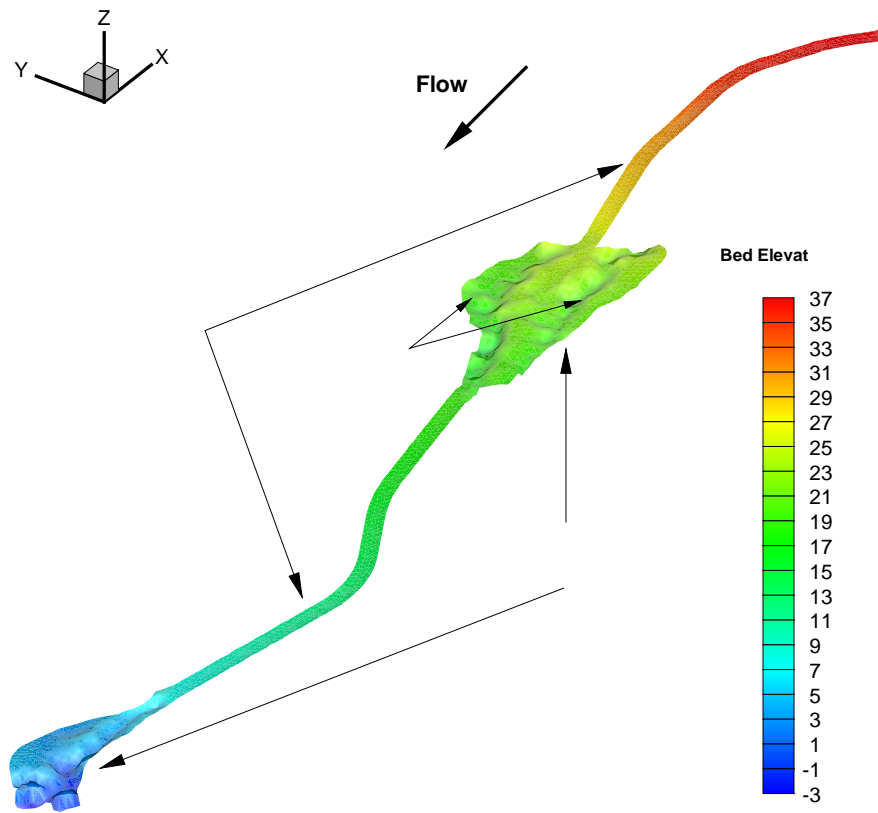grids. Two cases were modelled: one was using the original wall boundaries from field survey; the other one was using designed levees as wall boundaries. In the former one, total of 2442 elements were used in this 2 km long reach, while in the latter one 1874 elements were used. Constant discharge flow conditions were simulated and the time step of both computations is 0.1 second. Q = 1568.1 m^3/s represented the 50-year flood event based on the design hydrographs that were constructed for each river of the watershed, namely 1039.6 m^3/s and 528.5 m^3/s as inflow boundaries of Cañar and Patul Rivers respectively. The hydraulic structures were designed to drain 1100 m^3/s from the main river under this flood condition. Thus, the case of Q = 468.1 m^3/s was also modelled to study what could happen to the flow and sediment transport after the hydraulic structures were built.
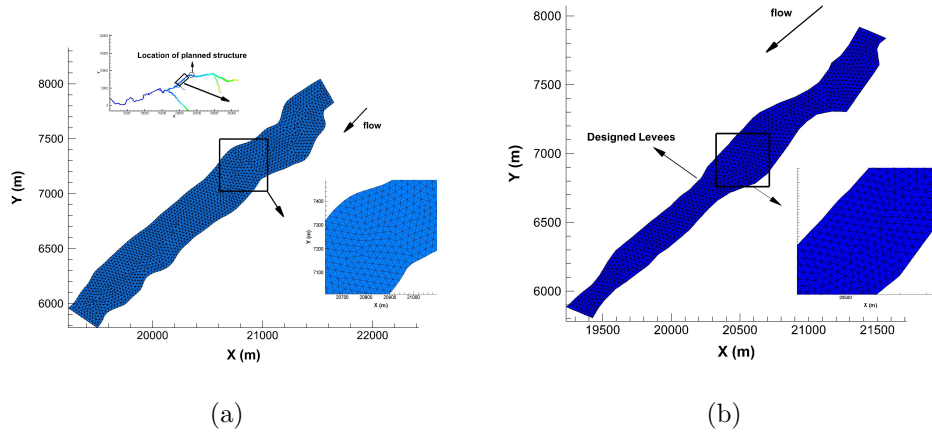
Figure 5.5: Computational domain and unstructured meshes in HydroSed2D model: (a) original boundaries; (b) designed levees as boundaries

The simulation domain for HydroSed2D applications started downstream of planned diversion dam and reaches to the confluence where Piedras River meets Cañar River (see figure 5.3). As discussed above, two simulation scenarios were modelled with constant inflow Q = 1568.1 m^3/s and Q = 468.1 m^3/s, respectively. The high discharge case simulated 50-year flood event that combined the inflows from Cañar and Patul Rivers; while the low discharge case represented the expected effect of hydraulic structures, which was designed to divert 1100 m^3/s flow into a by-pass channel in case of an upstream flood. The downstream water surface elevation boundary conditions were taken from the results of 1D HEC-RAS simulations. In rest of

the domain the water depth and flow velocity were evaluated based on upstream discharge and downstream water surface elevation conditions. Firstly, the flow-only simulations without considering sediment transport had been running until equilibrium states were reached.

The results of HydroSed2D simulations in terms of depth-averaged velocity magnitude and water depth for both scenarios are shown in figure 5.6. The code shows the capability to predict dry areas in low flow situations. Some dry areas can be seen clearly in the low discharge case especially near left bank (see figure 5.6c). In low discharge case, the water depth ranges between 0.5 m and 2 m in the reach while in high flow case it mostly changes between 2 m and 3 m. Similarly, flow velocities are reduced acutely in simulation where diversion dam is assumed to divert 1100 m^3/s of flow from this reach compared to high discharge case.
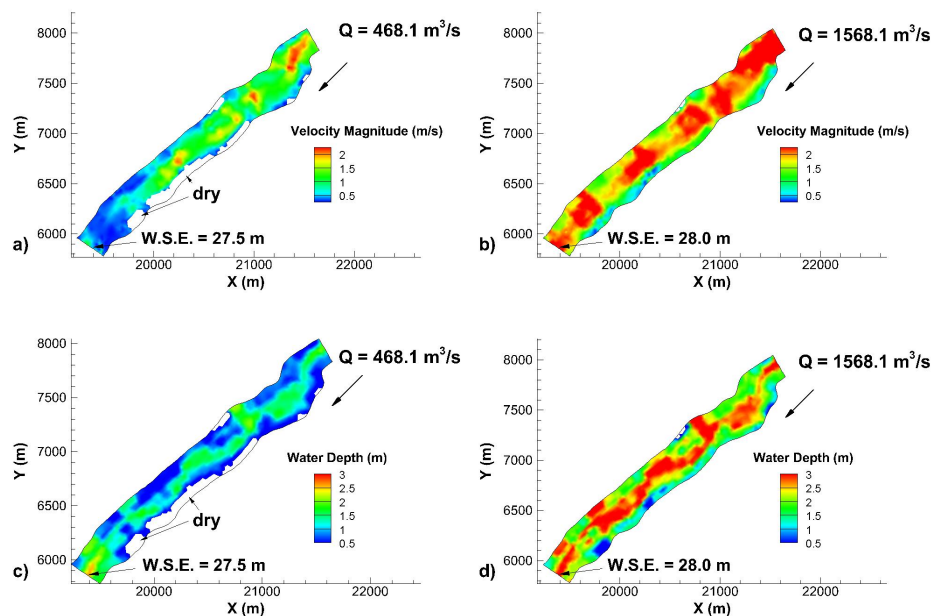
Figure 5.6: HydroSed2D simulation results of depth-averaged velocity magnitude and water depth

However, even though the dry areas can be seen in the case of low discharge in figure 5.6, flood areas still exist which may result in troubles during flood event. The model demonstrates that it is still necessary to design levees besides the construction of the diversion dam. Levees were designed to be placed downstream of the dam in the Cañar River to further prevent flooding in the region. In order to test the design of levees, another simulation with

designed levees as wall boundaries was modelled. The simulation run until reaching equilibrium state. In figure 5.7, the water surface elevation contours are shown together with the designed levees for low discharge case. In this simulation the locations of designed levees were taken as wall boundaries instead of the original boundaries. The elevation of the levees is shown using the same color scale as water surface elevation. The effectiveness of the levees could be assessed using simulation results in this reach. If one assumes that diversion dam works as designed, the numerical results show that the levees are high enough to avoid water inundation to flood plain. It is also shown that there is some space to lower or optimize the designed levees in order to cut down the cost of construction projects.

Figure 5.7: HydroSed2D simulation result of water surface elevation with the designed levees (represented by colourful squares)

Moreover, the sediment transport problem after building the structures was considered. The field survey data showed that the sediment particles in this domain were mainly gravel with the median size $D_{50} = 28.6$ mm. Therefore,
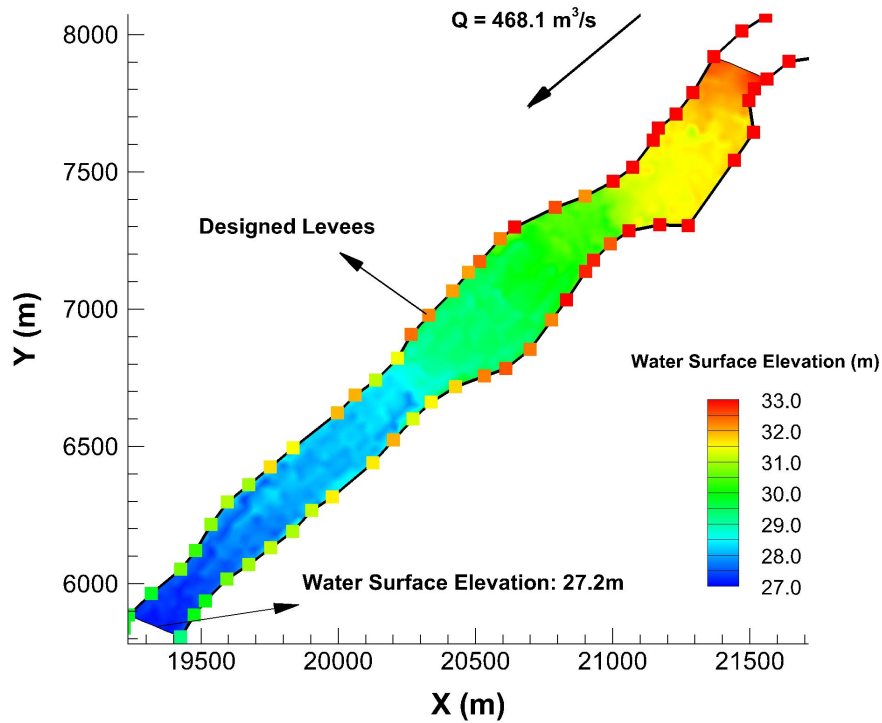
$$R_{ep} = \frac{\sqrt{gRDD}}{\upsilon} = 1944 \gg 37.0$$

Note that the García and Parker formula for suspended sediment transport was developed based on the sediment size data range from 0.09 mm to 0.44 mm, which was much less than 28.6 mm. The suspended sediment transport module was not applicable in this study domain. However, the Meyer-Peter and Muller formula for bedload transport has been verified with data for gravel ([13]), so only bedload transport of sediment was modelled in this case study. The equilibrium state in flow-only simulation was taken as initial conditions. The volume bedload transport rate per unit width q_b at time t = 1 hr is shown in figure 5.8. The black arrows in the river domain shows the direction of sediment bedload transport.
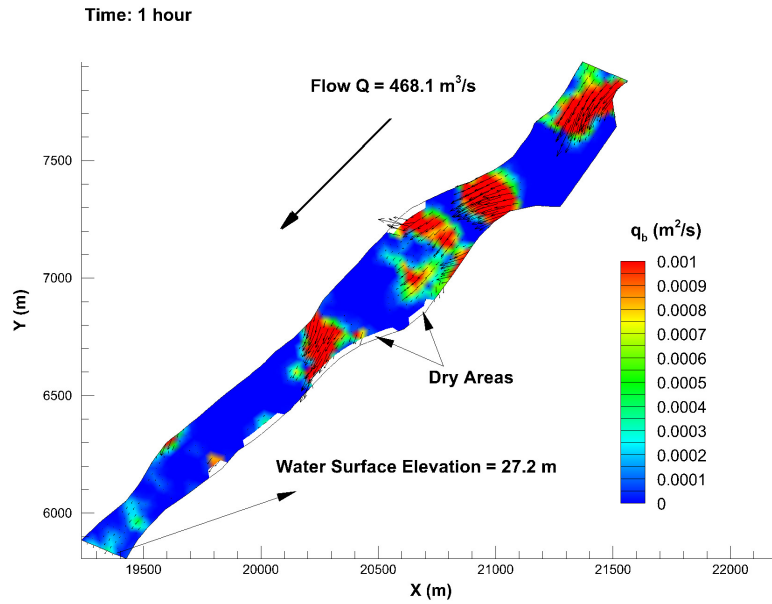
Figure 5.8: The volume bedload transport rate per unit width q_b

From figure 5.8, it is seen that in most areas the bedload transport rate is quite small. However, in the areas where the flow width is shrank, the transport rate is relatively much higher. Since it is actually the divergence of q_b which works for the evolution of bed elevation, one should notice that high change rate of bed elevation may happen at the edges of those high-q_b areas. Special attention or protection may be considered there.

5.3 Numerical Results of Case 2

Figure 5.4 shows the original bed elevation of the study domain surveyed by local researchers and engineers. During flooding events, some water will flow passing weirs which forms bypass flow and reduces the flow in the Cañar River. Since the bypass flow discharge may be very high and the sediment particle size in this area is quite small, the flow may be able to carry a large number of sediment downstream. However, the downstream of this area is so productive that people do not want it to be affected badly by sediment transport problems. Although the diversion can help solve the flooding problems in the Cañar River, it is necessary to make sure it will not destroy the drainage areas instead. Sediment transport problems are a big concern in this study domain. Therefore, the engineers designed two man-made lakes (see figure 5.4). When water flows into the lakes, the water velocities will be decreased and most of sediment is expected to deposit into those lakes.

5.3.1 Numerical simulations with original bed elevation

HydroSed model is applied to simulate the hydrodynamics under the condition of original bed elevation information of two lagoons. The meshes are shown in figure 5.9. The meshes are generated by using GAMBIT. There are totally 1887 nodes and the number of elements is 3266. The time step is 0.1 second. Mannings coefficient n is taken as 0.03. Q = 1100 m^3/s, which corresponds to 50-year flood event, is taken as upstream boundary condition and downstream boundary condition is that the water surface elevation equals to 2.25 m.

From the simulation results (see figure 5.10), it can be found that the water depth varies a lot inside the upstream lagoon. In order to verify the results, the 3D EFDC model is also applied to the same problem. The EFDC result is shown in figure 5.11. The comparison shows general agreement between each other. Due to the natural bed elevation in the upstream lagoon, the water depth will be relatively high at somewhere and very low at somewhere else. In that case, the function of the lagoon will not be fully developed. Meanwhile it is difficult to design the height of the levees.

Therefore, it is necessary to re-design the bed of the lagoon to be more
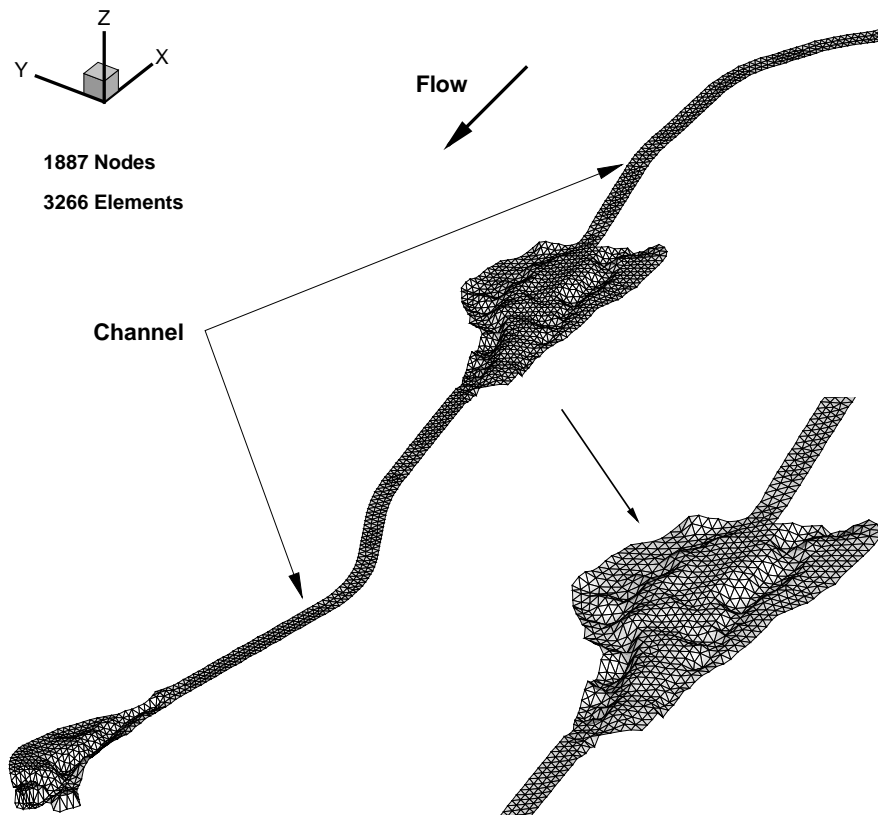
Figure 5.9: Computation meshes in HydroSed model with original bathymetry

regular. First, it will help design the height of the levees. Second, there should be always waterway connecting upstream channel and downstream channel. Third, it will maximize the function of the lagoon because we should take advantage of this area and use this area as much as possible.
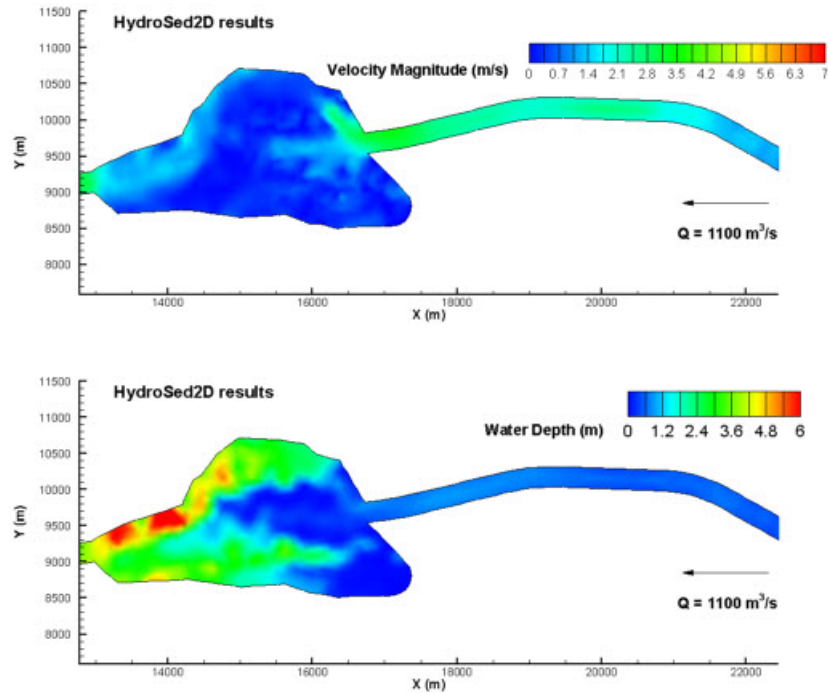
Figure 5.10: HydroSed results of depth-averaged velocity magnitude and water depth in the upstream lagoon area

5.3.2 Numerical simulations with new designed lagoon and channels

As explained above, the bed elevation of the lagoon is re-designed. Levees are also designed in order to separate the flow into three parts at the entrance of the lagoon (see figure 5.12).

The domain can be divided into two parts by the weir located at the downstream of lagoon so that two models are built by using HydroSed model. In the upstream part (part A), the meshes contain 7412 cells; in part B there are 1294 cells (see figure 5.13. The size of cells is smaller in part A in order to capture the effect of levees inside the lagoon.

60
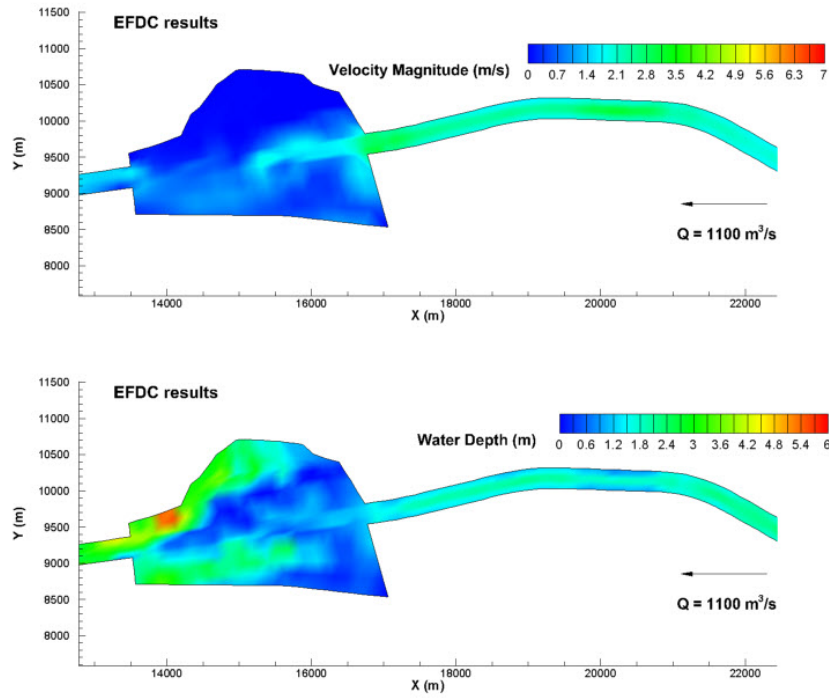
Figure 5.11: EFDC results of depth-averaged velocity magnitude and water depth in the upstream lagoon area

The upstream boundary condition for both parts is Q = 1100 m^3/s. For the upstream part, the water surface elevation equals to 22.34 m at downstream boundary according to the design of the weir. For the downstream part, the downstream boundary condition is still that the water surface elevation equals to 2.25 m. Regardless of sediment transport and bed evolution, the flow simulation results are shown in figure 5.14. The flow velocity magnitude in the channels is around 2 m/s. The water depth inside the upstream lagoon is around 1 m to 4.5 m, which is helpful for levees design. As expected, the flow velocity magnitude decreases dramatically when water flows into the lagoons.

The equilibrium state under flow-only condition is taken as the initial condition for sediment transport and bed evolution simulation. For bedload transport, Meyer-Peter and Muller formula is used.

The figure 5.15 shows that the upstream lagoon is very helpful for sediment deposition. The concentration of suspended sediment is reduced dramatically after a short distance in the lagoon. In the downstream channel, the water again takes sediment from the channel bed. When it reaches the downstream

61
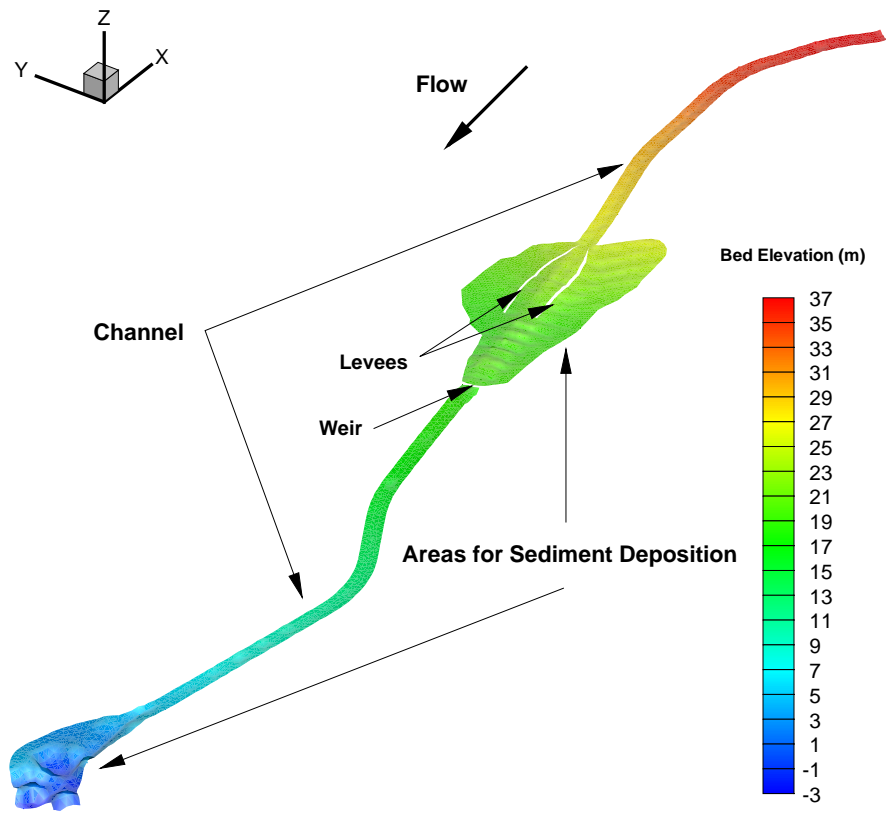
Figure 5.12: Bed elevation of the domain with new designed lagoon and levees

Part A

    7412 cells

Part B

    1294 cells
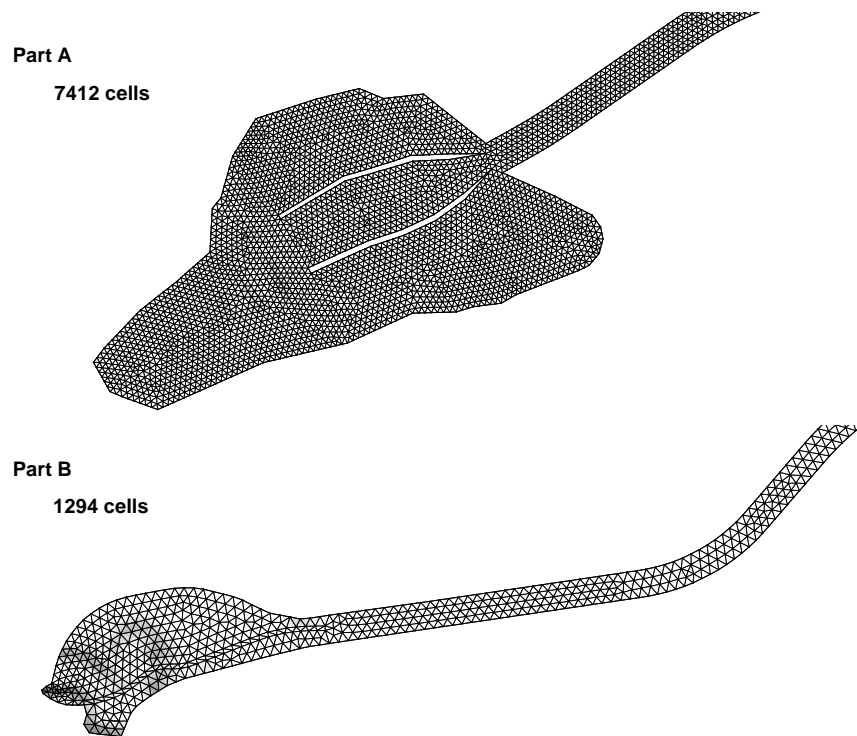
Figure 5.13: Computation meshes in HydroSed model
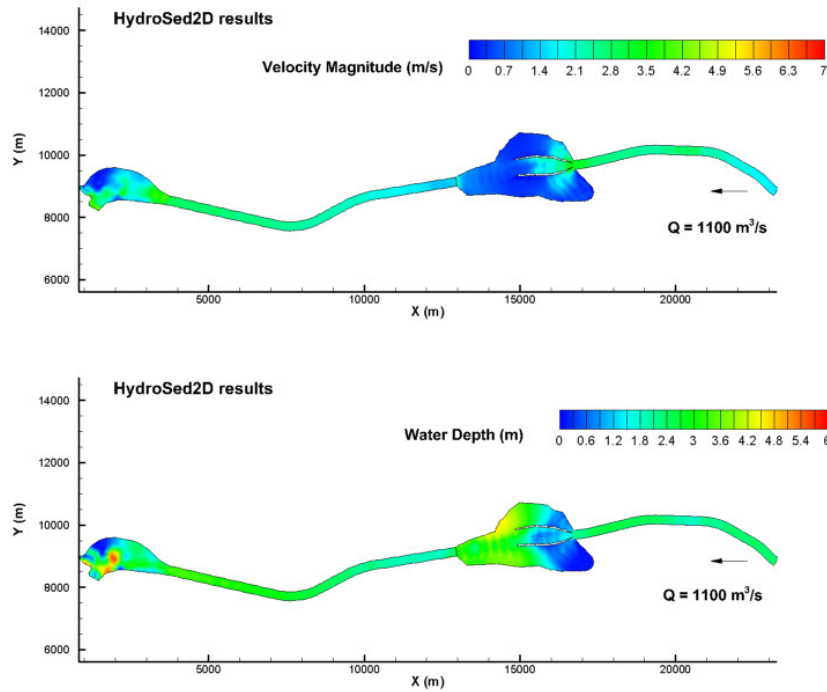
Figure 5.14: The results of flow velocity and water depth in HydroSed simulations

lake, the concentration (volume rate) can be as high as 0.1. In the downstream lagoon, the concentration is high inside the small channels which are designed for sediment to deposit. From the simulation, it shows that in the end of the domain the concentration is quite small.

The figures 5.16 and 5.17 show the change of bed elevation after certain time under the condition of flood flow Q = 1100 m^3/s. In the upstream part A, from the initial bed elevation, it is seen that in order to reduce the slope sequential steps are designed inside the lagoon. The results show those areas are obvious deposition area. On the contrary the entrance of the lagoon, especially the entrances to side channels, is easy-erosion area. In the downstream part B, the entrance also shows big erosion since the channel is narrowed down there. In the areas of designed channels, much deposition happens as expected. Also, there is much erosion happening on the bank of the channels because the domain is fully submersed under the condition of flood flow. Special protection should be applied because the bank slope is very big. However, the protection cannot be considered in the model.
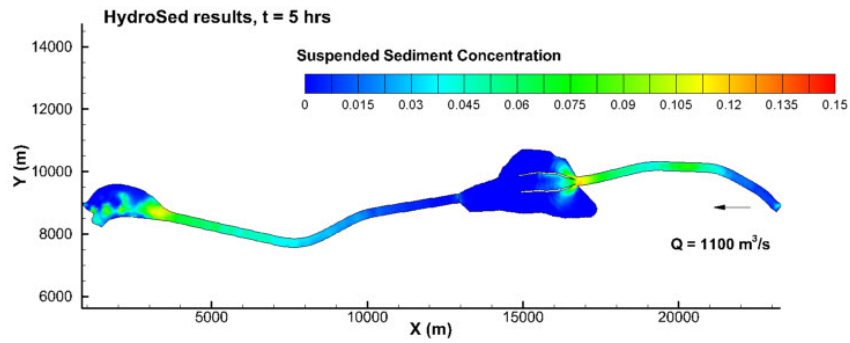
Figure 5.15: The concentration of suspended sediment at t = 5 hours
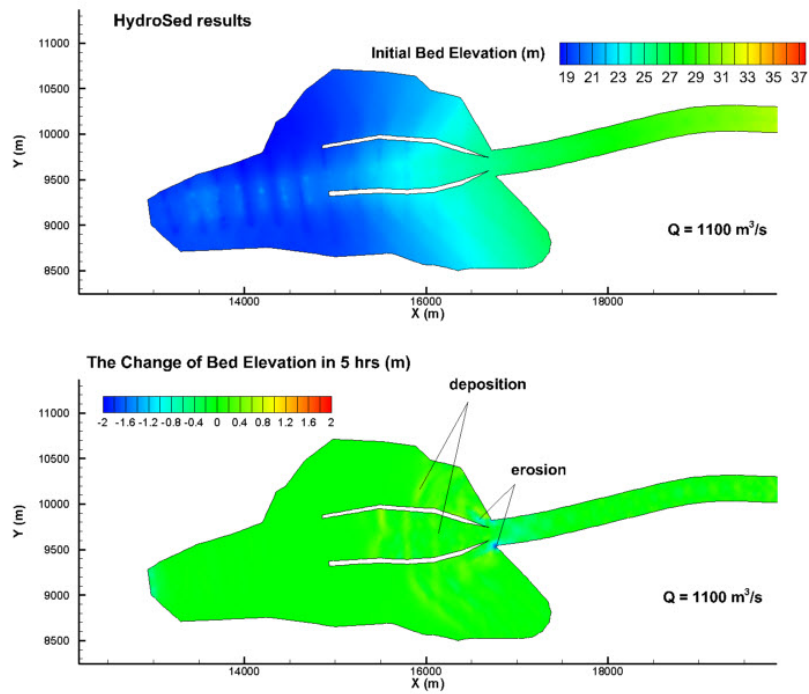
Figure 5.16: The change of bed elevation in part A after 5 hours
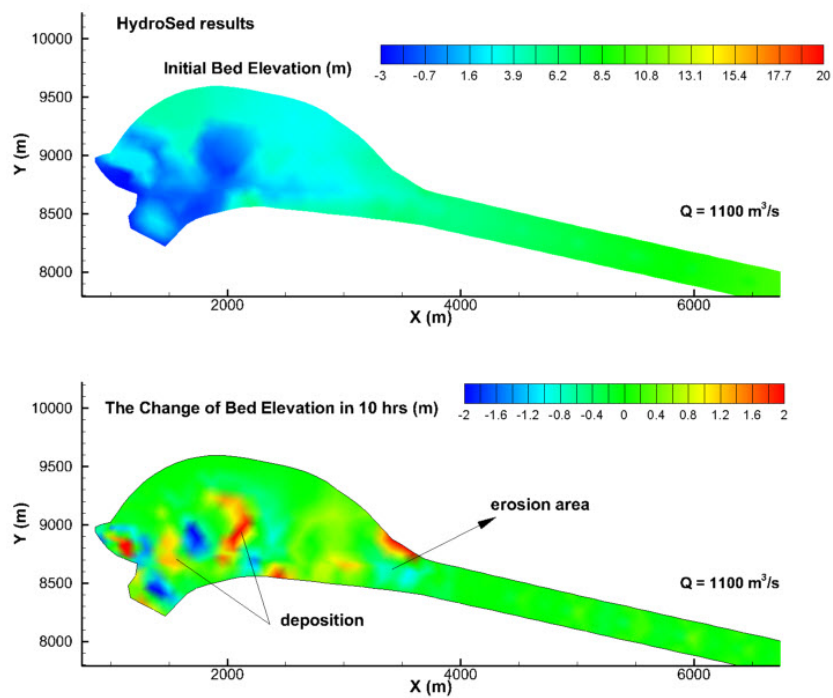
Figure 5.17: The change of bed elevation in part B after 10 hours

CHAPTER 6

CONCLUSIONS

The original HydroSedv1.0 model has been modified and improved so that the transport of contaminant and suspended sediment can be simulated. The new model has been tested by using several pure advection simulations and a dye-tracer study in the Chicago River. In the pure advection tests, numerical diffusion and oscillation are observed. By applying face-limiter approaches, the numerical accuracy is dramatically improved. The behaviours of different limiters are evaluated and discussed. The dye-tracer study in the Chicago River further proves the model's applicability in real-world projects. A widely used three-dimensional model EFDC is used for more comparisons.

The model is applied to study potential impacts of planned hydraulic structures in the Cañar River, Ecuador. The flow condition and potential sediment transport problems during floods are considered. The model is able to be a very useful tool for verifying and optimizing project designs.

In the end, the author would like to mention several ideas which may be future works. The turbulent model used currently is a simple 0-equation model, the depth-averaged parabolic model. More complicated and advanced turbulent models, such as $k - \epsilon$, may be applied. The change of water density is not considered in the existing model, so is water temperature. The term of water density ρ varying with water temperature and solute concentration may also be employed. Furthermore, as far as river morphodynamics is concerned, bank migration is another important problem besides bed evolution in meandering rivers. The author is considering taking advantage of the HydroSed model to do numerical studies of bank migration too.

APPENDIX A

COMPLEMENT OF USER'S MANUAL

A.1 Introduction

Dr. Xiaofeng Liu wrote a User's Manual for HydroSedv1.0 which can be downloaded at the following website:

http://sourceforge.net/projects/hydrosed2d/

One can also find the original code of HydroSedv1.0 in that package. In that manual, Dr. Liu concisely explained the numerical model and gave several examples simulated by using HydroSedv1.0. Also, some information about mesh generation and a tool code for interpolating bed elevation was introduced. Since modifications have been done in the new HydroSed model, the author think it is necessary to write this complement material for the previous User's Manual and explain more about how to operate the input files and some announcements which could be useful for users.

The users are recommended to read User's Manual for HydroSedv1.0 and the previous content of this thesis for better understanding the techniques inside the HydroSed model. In this appendix, the author tries to write from user's point of view in order to help users operate the model more easily and efficiently.

A.2 Mesh Generation and Interpolation Tool

Two kinds of mesh format can be read in HydroSed: Gambit neutral format and GMSH format ([37]). The boundaries need to be specified in the mesh file. Note that 1 for inlet boundaries, 2 for outlet boundaries and 3 for wall boundaries. For example, after generating meshes and specifying boundaries in Gambit, a ".neu" will be built. In Gambit v2.3.16, the boundary infor-

```
BOUNDARY CONDITIONS 2.3.16
                               inlet       1       2       0       6
      7479    3    1
      7486    3    2
ENDOFSECTION
 BOUNDARY CONDITIONS 2.3.16
                               outlet      1      10       0       6
      1372    3    1
      1376    3    3
      1422    3    3
      1437    3    3
      1449    3    3
      1472    3    3
      1478    3    3
      1482    3    1
      1480    3    1
      1433    3    1
ENDOFSECTION
 BOUNDARY CONDITIONS 2.3.16
                               wall        1    2126       0       6
      4947    3    2
      4939    3    1
        26    3    3
        24    3    3
```

Figure A.1: Boundary information in Gambit mesh file

mation appears in the end of the mesh file (see figure A.1). Originally, all boundaries are flagged as "6". They need to be changed to 1, 2 or 3 as mentioned above.

Usually when generating meshes in Gambit or GMSH, users may not consider the z coordinate, e.g. bed elevation, and focus on 2D horizontal meshes. In a normal mesh file (see figure A.2), the number of total nodes and elements and other information are firstly introduced. Then from line 10, one can see that only x and y coordinates are shown. However, before reading this mesh file into the model, the z coordinate need to be added. Usually users may have field survey data for real-world project or some coordinates information at representative locations for conceptual or experimental channels. What need to be done is to do interpolation from known data to the computation nodes. A useful tool code written in FORTRAN95 is provided together with the HydroSed model in the downloadable package. The author further modified and optimized the code so that one can choose how many points are needed to do interpolation for each node and one can use either direct averaging or distance-weighted averaging in which 1/L is taken as weighting parameter so that the nearer point has a larger weight. Moreover, the

```
 1          CONTROL INFO 2.3.16
 2  ** GAMBIT NEUTRAL FILE
 3  ChicagoRiver4
 4  PROGRAM:              Gambit     VERSION:   2.3.16
 5   May 2011
 6       NUMNP      NELEM      NGRPS     NBSETS     NDFCD     NDFVL
 7       5057       7974          1          3         2         2
 8  ENDOFSECTION
 9     NODAL COORDINATES 2.3.16
10         1  8.02771386719e+003  1.27050449219e+004
11         2  7.45420605469e+003  1.24598457031e+004
12         3  7.57342382813e+003  1.25110410156e+004
13         4  7.68385888672e+003  1.25584638672e+004
14         5  7.79723681641e+003  1.26031611328e+004
15         6  7.90397900391e+003  1.26505361328e+004
```

Figure A.2: Coordinates information in Gambit mesh file

```
 1  -13.1924     -18.48424    -6.9604648
 2  -10.8624     -17.92424    -6.7304648
 3  -14.8424     -17.77424    -6.9304648
 4  -9.2124 -17.44424    -6.8404648
 5  -16.5124     -17.02424    -6.8404648
```

Figure A.3: Example of the dem.dat file

code is able to interpolate Manning's coefficient for each node. In the previous model, the Manning's coefficient n is always taken as constant which is specified in the master input file. Now n can vary in different locations too. This tool contains four ".f90" files, namely "module.f90", "DEMInterpolation.f90", "readGambitMesh.f90" and "readGMSHMesh.f90". "DEMInterpolation.f90" is the main program file and "module.f90" is the file where different options and parameters need to be specified (see figure A.4). The input files needed are mesh file and a "dem.dat" file in which the topography database is saved (see figure A.3). x, y and z coordinates of each point is put separately by blank space in one line.

In figure A.4, users can specify the maximum number of computation nodes, elements and boundary edges in line 4. It is recommended to use a bigger number than the minimum requirement of meshes.

In line 7, the maximum edges of each element is specified. For example, it is 3 when triangular meshes are used, or 4 when rectangular meshes are used.

In line 10, the name of the old mesh file and the processed mesh file is filled in.

```
1    MODULE   COMMON_MODULE
2
3        integer*4 maxnodes_, maxfaces_, maxboundaryedges_
4        parameter(maxnodes_ = 10000, maxfaces_ = 50000, maxboundaryedges_ = 3000)
5
6        integer*4 ELEDGES        !maximum edges for each cell
7        parameter(ELEDGES=3)
8
9        CHARACTER*80 NEUFILE, NEWNEUFILE, tempchar
10       parameter(NEUFILE = 'Ecuador_lagoon.neu', NEWNEUFILE = 'Ecuador_lagoon_new.neu')
11
12       integer nFileType  !1: GMSH  2: Gambit Neutral
13       parameter(nFileType = 2)
14
15       integer,parameter::nDEMPoints = 20930
16
17       !1 to use distance-weighted averaging; 2 to do direct averaging
18       integer,parameter::IFWeight=1
19
20       !how many points are used to evaluate the node elevation
21       integer,parameter::nPoint=20
22
```

Figure A.4: Parameters in the interpolation tool

```
1   "runtype: 0-run from start, 1-run from restart"
2   0
3   "reload file name"
4   re60.dat
5   "dt","nts","ts","tstop"
6   0.1,10,68400,259200
7   "g","visc","beta(limiter parameter)","n","turb","alphat"
8   9.8,1.0e-6,1,0.02,0,0.2
9   "drydeep","mindeep"
10  0.01,0.001
11  "inlet_condition_control: 1-given h, 2-given u, 3-given q"
12  3
```

Figure A.5: Example of master input file ctr.txt

In line 13, 1 means GMSH file and 2 means Gambit file.

In line 15, the total number of points in the database, e.g. dem.dat file, is specified.

In line 18, 1 means using distance-weighted averaging; 2 means using direct averaging.

In line 21, one can specify how many points from database will be used to do interpolation for each computation node.

A.3   The Master Input File (ctr.txt)

The master input file of the HydroSed model is the file of "ctr.txt". One example is shown in figures A.5, A.6 and A.7.

In line 2, 0 means running the model from start, while 1 means running

```
13  "inletH inletUB inletVB inletQ"
14  -0.7 -0.1 0.0 65.0
15  "outlet_condition_control(for downstream): 1-given h, 2-given u,
16  1
17  "outletH(WSE) outletUB outletVB outletQ"
18  -0.7 1 0.0 -1500.0
19  "deltaT for output results (deltaT_output)"
20  6000
21  "deltaT for restart results (deltaT_restart)"
22  432000
23  "sediment control","bedload control","suspended load control"
24  0 0 0
```

Figure A.6: Example of master input file ctr.txt (continued)

from restart which needs read a reload file named in line 4.

In line 6, some parameters about time steps and starting/ending time are specified. "dt" is the time step in the calculation of flow. The time scale of bed evolution is normally much bigger than that of flow. In order to speed up the simulation, one can use a bigger time scale for sediment transport. "nts" = 10 means the time step for sediment transport is 10 times bigger than that for flow. "ts" is the starting time; "tstop" is the ending time of the simulation.

In line 8, the gravity acceleration g, water viscosity ν are specified firstly. The limiter parameter β can be chosen. 1 corresponds to minmod limiter and 2 means Roe's superbee limiter. One can also try other numbers between 1 to 2, like 1.5. "n" is Manning's coefficient. If n >0, a constant Manning's coefficient will be used for all nodes. Otherwise, the model will read Manning's coefficients for different modes automatically from the mesh input file. "turb" = 0 means no turbulent model is considered; while 1 means the depth-averaged parabolic turbulent model will be applied. "alphat" is the parameter α_T used in the turbulent model.

In line 10, "drydeep" and "mindeep" are used to deal with wet/dry. When the water depth is less than "drydeep", the computation cell will be taken as dry area and its edges will be taken as wall boundaries.

In line 12, three options of inlet boundary conditions can be chosen. 1 means the water height is given; 2 means the velocities are given; 3 means inflow discharge is given.

In line 14, constant inlet boundary conditions can be specified according to the option chosen in line 12.

In line 16, similarly as inlet boundary, the types of outlet boundary con-

```
25  "mesh file format: 1. gmsh  2. gambit neutral"
26  2
27  "mesh file name"
28  "ChicagoRiver5_new.neu"
29  "q-t_control","q-tfilename"
30  1 "qt.txt"
31  "h-t_control","h-tfilename"
32  1 "ht.txt"
33  "initial condition: wse, u, v"
34  -0.7 0.0 0.0
35  "transportcontrol discoefcontrol Dxx Dxy Dyx Dyy","ctfile"
36  1 2 0.07 0.01 0.01 0.07 "ct.txt"
```

Figure A.7: Example of master input file ctr.txt (continued)

ditions can be specified. Also, constant condition can be further specified in line 18.

In line 20, one can choose how often the output file will be generated. The format of output files is ".dat" and directly readable in the software Tecplot. In line 22, similarly, one can specify the frequency for outputting output files for the purpose of running form restart.

In line 24, one can choose if sediment transport module is activated. Furthermore, one can activate bedload transport only or suspended load only. As always, 0 means inactivation and 1 means activation.

In line 26, 1 means the format of mesh file is GMSH file; 2 means it is Gambit neutral file. The name of mesh file should be written in line 28.

In line 30 and 32, it offers the option for applying varying boundary conditions. For example, in line 30, one can set 1 to read varying discharges as upstream boundary condition. Likewise, setting 1 in line 32 can allow users ready varying water height as downstream boundary condition.

In line 34, one can set up initial condition including water surface elevation and velocities.

In line 36, "transportcontrol" equals to 1 corresponding to activation of contaminant transport module. "discoefcontrol" equals to 1 corresponding to constant dispersion coefficients; 2 corresponding to applying formulas to compute dispersion coefficients. In "ct.txt" file, the location of injection and flow rate can be specified.

```
1  2600    !rhos
2  1000    !rhow
3  0.003   !diam
4  0.3     !porosity
5  0.047   !thita_cri_b
6  0.52    !angleofRepose
7  0       !C_slope
8  2       !sediment transport rate formula: 1-MPM, 2-Grass
9  0.001 3 !A and m value for Grass sediment transport rate formula
10
```

Figure A.8: Sediment properties input file sediment.txt

A.4   Additional Input Files

A.4.1   Sediment Properties Input (sediment.txt)

In figure A.8,

   Line 1 "rhos" : the sediment density;

   Line 2 "rhow" : the water density;

   Line 3 "diam" : the sediment particle diameter;

   Line 4 "porosity" : the bed porosity, λ_p;

   Line 5 "thita_cri_b" : the critical Shields number for bed load, τ_c^*;

   Line 6 "angleofRepose" : the angle of repose for sediment;

   Line 7 "C_slope" : a constant for slope effect in bedload transport;

   Line 8 : bedload transport formulas: 1 - Meyer-Peter and Muller's formual;
2 - Grass' formula;

   Line 9 : parameters A and m in Grass' formula;

A.4.2   qt.txt

This input file provides inflow discharges varying with time. It is worthy mentioning that the name of the file can be changed in line 30 in the master input file. In the figure A.9, the total number of time-discharge pair is specified firstly. Then, in each line, a pair of time and discharge is provided. The unit of time is hour; the unit of discharge is m^3/s.

```
1  433
2  0.166666667 0.914727218
3  0.333333333 17.5557364
4  0.5 59.92483335
5  0.666666667 66.13711452
6  0.833333333 26.83727269
7  1    50.75823212
8  1.166666667 32.0974326
9  1.333333333 19.66874451
```

Figure A.9: Example of input file qt.txt

```
1  7
2  0.0 −0.75
3  12.0 −0.625
4  30.0 −0.7
5  48.0 −0.85
6  54.0 −0.9
7  72.0 −0.7
8  100.0 −0.7
9
```

Figure A.10: Example of input file ht.txt

```
 1  !Inject Location Information
 2  8
 3  5263
 4  5264
 5  5265
 6  5266
 7  5866
 8  5867
 9  6070
10  6071
11  !Time Series
12  6
13  0.0 0.0
14  19.849 0.0
15  19.85 0.67965
16  28.7833 0.67965
17  28.7834 0.0
18  100.0 0.0
```

Figure A.11: Example of input file ct.txt

A.4.3   ht.txt

The figure A.10 shows the input file which provides water height varying with time. The format is the same as the file of qt.txt. The unit of time is hour; the unit of water surface elevation is meter.

A.4.4   ct.txt

The figure A.11 shows an example of ct.txt file. There are two parts in this file: one is to specify the injection location; the other one is to provide varying inflow rate. 8 at line 2 and 6 at line 12 correspond to the total number of location and time-flow rate pairs separately. The location is expressed as the computation element code which can be found in the mesh input file. The unit of time is hour. The contaminant flow rate is equal to $Q_w C$. Q_w represents water discharge and C represents the contaminant concentration in the water injected.

A.5 Compiling and Executing the Code

Compaq Visual Fortran v6.6 compiler in Windows system and Intel Fortran v10.1.013 compiler in Linux system have both been tested and working fine.

REFERENCES

[1] R. C. MacArthur, C. R. Neill, B. R. Hall, V. J. Galay, and A. B. Shvidchenko, "Overview of sedimentation engineering," in *Sedimentation Engineering Processes, Measurements, Modeling and Practice*, M. H. García, Ed. Reston, Va: Am. Soc. Civ. Eng., 2008, ch. 1, pp. 1–4.

[2] X. Liu and M. H. García, "Numerical simulation of local scour with free surface and automatic mesh deformation," in *Proceedings of World Environmental and Water Resource Congress*, Omaha. NE, 2006.

[3] M. Sladkevich, A. N. Militeev, H. Rubin, and E. Kit, "Simulation of transport phenomena in shallow aquatic environment," *Journal of Hydraulic Engineering*, vol. 126, pp. 123–136, Feb. 2000.

[4] W. Wu, "Depth-averaged two-dimensional numerical modeling of unsteady flow and nonuniform sediment transport in open channels," *Journal of Hydraulic Engineering*, vol. 130, pp. 1013–1024, Oct. 2004.

[5] J. Hudson and P. K. Sweby, "A high-resolution scheme for the equations governing 2d bed-load sediment transport," *International Journal for Numerical Methods in Fluids*, vol. 47, pp. 1085–1091, 2005.

[6] J. Murillo, J. Burguete, P. Brufau, and P. García-Navarro, "Coupling between shallow water and solute ow equations : analysis and management of source terms in 2D," *International Journal for Numerical Methods in Fluids*, vol. 49, pp. 267–299, 2005.

[7] J. Murillo, P. García-Navarro, and J. Burguete, "Analysis of a second-order upwind method for the simulation of solute transport in 2D shallow water flow," *International Journal for Numerical Methods in Fluids*, vol. 56, pp. 661–686, 2008.

[8] M. J. Castro Díaz, E. D. Fernández-Nieto, A. M. Ferreiro, and C. Parés, "Two-dimensional sediment transport models in shallow water equations. A second order finite volume approach on unstructured meshes," *Comput. Methods Appl. Mech. Engrg.*, vol. 198, pp. 2520–2538, 2009.

[9] I. Kimura, S. Onda, T. Hosoda, and Y. Shimizu, "Computations of suspended sediment transport in a shallow side-cavity using depth-averaged 2D models with effects of secondary currents," *Journal of Hydro-environment Research*, vol. 4, pp. 153–161, 2010.

[10] K. Nadaoka and H. Yagi, "SHALLOW-WATER TURBULENCE MODELING AND HORIZONTAL LARGE-EDDY COMPUTATION OF RIVER FLOW," *Journal of Hydraulic Engineering*, vol. 124, no. 5, pp. 493–500, 1998.

[11] X. Liu, B. Landry, and M. H. García, "Two-dimensional scour simulation based on coupled model of shallow water equations and sediment transport on unstructured meshes," *Coastal Engineering*, vol. 43, pp. 357–372, 2008.

[12] J. W. Elder, "The dispersion of marked fluid in turbulent shear flow," *J. Fluid Mech.*, pp. 544–560, 1959.

[13] M. H. García, Ed., *Sedimentation Engineering Processes, Measurements, Modeling and Practice*. Reston, Va: Am. Soc. Civ. Eng., 2008.

[14] A. J. Grass, "Sediment transport by waves and currents," SERC London Center for Marine Technology, Tech. Rep. FL29, 1981.

[15] E. Meyer-Peter and R. Muller, "Formulas for bedload transport," in *Proceedings of the 2nd Congress, IAHR*, Stockholm, 1948, pp. 39–64.

[16] G. Parker, M. H. García, Y. Fukushima, and W. Yu, "Experiments on turbidity currents over an erodible bed," *Journal of Hydraulic Research*, vol. 25, pp. 123–147, 1987.

[17] M. H. García and G. Parker, "Entrainment of bed sediment into suspension," *Journal of Hydraulic Engineering*, vol. 117, pp. 414–435, 1991.

[18] M. H. García and G. Parker, "Experiments on the entrainment of sediment into suspension by a dense bottom current," *Journal of Geophysical Research (oceans)*, vol. 98, pp. 4793–4807, 1993.

[19] Z. Cao, R. Day, and S. Egashira, "Coupled and decoupled numerical modeling of flow and morphological evolution in alluvial rivers," *Journal of Hydraulic Engineering*, vol. 128, pp. 306–321, 2002.

[20] P. L. Roe, "Approximate riemann solvers, parameter vectors, and difference schemes," *Journal of Computational Physics*, vol. 43, pp. 357–372, 1981.

[21] P. L. Roe, "Characteristic based schemes for the euler equations," *Annual Review of Fluid Mechanics*, vol. 18, pp. 337–365, 1986.

[22] S. K. Godunov, "A difference method for numerical calculation of discontinuous solutions of the equations of hydrodynamics," *Math. Sbomik*, vol. 47, pp. 271–306, 1959.

[23] R. J. LeVeque, *Finite Volume Methods for Hyperbolic Problems*. Cambridge, UK: Cambridge University Press, 2002.

[24] K. Anastasiou and C. T. Chan, "Solution of the 2d shallow water equations using the finite volume method on unstructured triangular meshes," *International Journal for Numerical Methods in Fluids*, vol. 24, pp. 1225–1245, 1997.

[25] J. Shen, "A one-stop reference source for comprehensive, up-to-date information on biology of silver, largescale silver and bighead carps and environmental risk assessment," *Environ. Biol. Fish*, vol. 84, pp. 341–344, 2009.

[26] J. M. Hamrick, "A three-dimensional environmental fluid dynamics computer code: theoretical and computational aspects," The College of William and Mary, Virginia Institute of Marine Science, Special Report 317, 1992.

[27] S. Sinha, X. Liu, and M. H. García, "Three-dimensional hydrodynamic and water quality modeling of a cso event in bubbly creek, chicago, il," in *Riverflow-2010 Conference Proceeding*, Braunschweig, Gernany, 2010, pp. 1556–1564.

[28] X. Liu and M. H. García, "Numerical simulation of density current in chicago river using environmental fluid dynamics code (efdc)," in *Proceedings of the World Environmental and Water Resources Congress 2008*, Honolulu, Hawaii, 2008.

[29] Z. G. Ji, G. Hu, J. Shen, and Y. Wan, "Three-dimensional modeling of hydrodynamic processes in the st. lucie estuary. estuarine," *Coastal and Shelf Science*, vol. 73, pp. 188–200, 2007.

[30] Z. G. Ji, G. Hu, J. Shen, and Y. Wan, "Numerical study on salinity stratification in the oujinag river estuary," *Journal of Hydrodynamics*, vol. 21, pp. 835–842, 2009.

[31] Q. R. Kong, C. B. Jiang, J. J. Qin, and B. Guo, "Sediment transportation and bed morphology reshaping in yellow river delta," *Sci. China Ser. E-Tech. Sci.*, vol. 52, pp. 3382–3390, 2009.

[32] G. L. Mellor and T. Yamada, "Development of a turbulence closure model for geophysical fluid problems," *Rev. Geophys. Space Phys.*, vol. 20, pp. 851–875, 1982.

[33] B. Galperin, L. H. Kantha, S. Hassid, and A. Rosati, "A quasi-equilibrium turbulent energy model for geophysical flows," *Journal of Atmos. Sci.*, vol. 45, pp. 55–62, 1988.

[34] H. B. Fischer, J. Imberger, R. C. Y. Koh, E. J. List, and N. H. Brooks, *Mixing in Inland and Coastal Waters.* London, UK: Academic Press, 1979.

[35] H. E. Center, "Hec-ras (river analysis system) reference manual," US Army Corps of Engineers, Davis CA, Tech. Rep., 2010.

[36] R. A. Wurbs and W. P. James, Eds., *Water Resources Engineering.* New Jersey, USA: Prentice Hall, 2002.

[37] C. Geuzaine and J.-F. Remacle, "Gmsh: a three-dimensional finite element mesh generator with built-in pre- and post-processing facilities," *International Journal for Numerical Methods in Engineering*, vol. 79, pp. 1309–1331, 2009.